Hybrid Nanometal Morphing Structures

by

Nicholas Ewaschuk

A thesis submitted in conformity with the requirements
for the degree of Master of Applied Science
Graduate Department of Aerospace Science and Engineering
University of Toronto

© Copyright 2021 by Nicholas Ewaschuk

Abstract

Hybrid Nanometal Morphing Structures

Nicholas Ewaschuk
Master of Applied Science
Graduate Department of Aerospace Science and Engineering
University of Toronto
2021

The demand for increasing the efficiency of aircraft has led to the pursuit of improved and novel structures. Hybrid structures with morphing capabilities aim to address this through the use of materials with high specific strength, improved manufacturing techniques, and the ability to change shape during flight. A quadrotor propeller was chosen as a proof of concept design for a morphing hybrid structure. This thesis investigates the implementation of morphing via mechanical actuation into various propeller designs, weighing the benefits and tradeoffs for each. A NACA 2412 airfoil was optimized for two separate flight conditions, and various designs were conceptualized for implementation. A design was selected for a finite element analysis to determine the viability of morphing within the structure.

Contents

1 Introduction **1**

1.1 Motivation . . . 1

1.2 Thesis Outline . . . 2

2 Literature Review **3**

2.1 Early Morphing Designs . . . 3

2.2 Morphing Structures . . . 5

2.3 Compliance and Compliant Mechanisms . . . 6

2.4 Actuators . . . 6

2.5 Nanometal Hybrid Structures . . . 8

3 Aerodynamic Optimization **10**

3.1 Blade Element Momentum Theory . . . 10

3.1.1 Inclusion of Motor and Weight . . . 12

3.1.2 Assumptions . . . 13

3.2 Vortex Panel Method . . . 13

3.3 Optimization Algorithm . . . 15

3.4 Assigned Conditions and Properties . . . 15

3.5 Optimization Results . . . 16

4 Design Concepts **21**

4.1 Design 1 - Solid Body . . . 22

4.2 Design 2 - Rigid Wireframe Body . . . 26

4.3 Design 3 - Rotating Wireframe Body . . . 30

4.4 Design Discussion . . . 36

5 Finite Element Model **37**

5.1 Model Details . . . 37

5.2 Double Wireframe Section Morphing Analysis . . . 41

5.2.1 Analysis Setup . . . 41

5.2.2 Double Wireframe Section Morphing Results . . . 42

5.2.3 Mesh Convergence Analysis . . . 44

5.3 Full Model Analysis . . . 49

5.3.1 Analysis Setup . . . 49

5.3.2 Full Model Results 49

6 Conclusions **55**

Bibliography **57**

List of Tables

3.1 Twist angle results at discrete sections of the propeller 17
3.2 Twist angle difference between hovering and forward flight 17
3.3 Operating parameters at specified flight condition 18

5.1 Cartesian coordiantes for NACA 2412 profile 38
5.2 Cartesian coordiantes for the first discrete section after transformation 40
5.3 Twist angle changes with varying cutout placements 44
5.4 Von Mises stress values for varying mesh densities 46
5.5 Change in Von Mises stress for varying mesh densities 47
5.6 Pressures applied to full propeller model and equivalent force 51
5.7 Twist angles before and after actuation for each wireframe section 54

List of Figures

2.1 Overview of morphing designs in aircraft 4
2.2 Single-layered PMHT with vacancy at the centre 5
2.3 Examples of various compliant mechanisms 6
2.4 Stroke-Force curve for an actuator 7

3.1 Visualization of velocities for blade element momentum theory 12
3.2 Illustration of the vortex panel method on an airfoil 14
3.3 NACA 2412 airfoil 16
3.4 Optimized twist angle profiles 18
3.5 Calculated pressure distribution of NACA 2412 airfoil at $\alpha = 5.5°$ 19
3.6 XFOIL pressure distribution of NACA 2412 airfoil at $\alpha = 5.5°$ 19
3.7 Propeller profiles generated at discrete sections 20
3.8 Lift distribution across propeller span 20

4.1 Isometric view showing top side of propeller blade with three actuator strips 22
4.2 Isometric view showing bottom side of propeller blade with two actuator strips 23
4.3 Top view of propeller blade with 3 actuator strips 23
4.4 Side view at root of propeller blade showcasing thin strip of an actuator on the top side . 24
4.5 Section view of hollowed propeller blade showing an embedded actuator and slot for electrical connections 25
4.6 Isometric view showing top side of the wireframe propeller blade 27
4.7 Top view of the wireframe propeller blade 27
4.8 Side view showing highlighting the wireframe sections 28
4.9 Side view showing a single wireframe section with a section removed for actuator placement 28
4.10 Side section view showing a hollowed out single wireframe section, highlighting potential electrical connection placement 29
4.11 Isometric view of the rotating wireframe design 31
4.12 Top view of the rotating wireframe design 31
4.13 Side view of the rotating wireframe design 32
4.14 Isometric view of a wireframe section showing protrusions on the connecting bar 32
4.15 Isometric view of the cap showing the cutout for the actuator 33
4.16 Isometric view of a wireframe section showing the assembly with the caps 33
4.17 Isometric view of the hollowed central connecting rod with a slotted section added 35
4.18 Isometric view of a the cap with a slot cut out 35

5.1 NACA 2412 plotted coordinates 39
5.2 First discrete section plotted coordinates after transformation 39
5.3 Meshed double wireframe section showing the location for the actuator 41
5.4 Load state for double wireframe section 42
5.5 Stress state from morphing for the double wireframe section 43
5.6 Boundary conditions applied to the double wireframe section 45
5.7 Plot of Von Mises stress values vs the number of elements for that simulation 46
5.8 Percent change in Von Mises stress of simulations for consecutive meshes 47
5.9 Stress state for the meshed wireframe model with 127543 elements 48
5.10 View of mesh for the full propeller model 49
5.11 Boundary conditions for the full propeller model 50
5.12 Loads applied to the full propeller model 50
5.13 Isometric view of full propeller after actuation 52
5.14 Top view of full propeller after actuation 52
5.15 Section view cut showing inner surface containing maximum stress location 53
5.16 Isometric view of propeller an order of magnitude lower stress limit 53
5.17 Section view cut with a single order of magnitude lower stress limit 54

Chapter 1

Introduction

1.1 Motivation

With the ever-increasing pressure for emission reduction across all technology sectors, the importance of reducing fuel consumption by increasing efficiency is very high. In the year 2017, civil aviation accounted for 859 million tonnes of CO_2, approximately 2% of man-made emissions [2] With the baseline projections of CO_2 emissions from civil aircraft expected to double between 2019 and the late 2030s, a lot must be done in order to meet the emission reduction goals through technological improvements of 1.5% per year [26].

Within aircraft design, there are many potential areas to focus on in order to improve fuel efficiency. This can be done through better engine design, structural efficiency improvements, or better aerodynamic design for various parts such as wings, flaps, or landings gears, to name a few. Other potential ways to reduce fuel consumption would be reimagining the conventional tube and wing design for civil aircraft, and developing better fuels. This thesis, however, will be focusing on the structural aspect of aircraft.

Within aircraft structure design, there are multiple methods to improve fuel efficiency for an aircraft. One method is to use more mass-efficient structures such as cellular solids in order to reduce weight but maintain strength. Another is to use more lightweight materials and advanced materials. For example, the Boeing-787 has nearly 50% of its airframe comprising of composites by weight, increased drastically over the 11% of the Boeing-777 [5]. These advanced materials include, but are not limited to, polymer matrix ceramic composites, metal matrix composites, composite sandwich panels, and polymer aerogels.

Another potential way of improving fuel efficiency is through the use of morphing technology. Morphing, in an aerospace context, can be defined as a set of technologies that increase a vehicle's performance by manipulating certain characteristics to better match the vehicle state to the environment and task at hand [31]. Although this is a very broad definition, there are many cases to help illustrate this concept. One example is the use of mechanical actuation in order to change the sweep of a wing. Another is the use of pneumatic actuators in combinations with multiple wing panels to create a telescopic wing, creating the ability to have a variable span wing. There are many potential applications of morphing, with even more possible methods that can be implemented. This thesis will focus on combining efficient structures and morphing capabilities with the goal of improved aerodynamic efficiencies in order to reduce fuel consumption.

1.2 Thesis Outline

The purpose of this work is to show the viability of a morphing structure using a 3D printed polymer substrate with an electrodeposited nanometal coating. While none of these technologies are new, the combination of them is novel. Chapter 2 will provide some details of past morphing designs in aircraft, and discuss the details of the technologies and concepts required in order to make a functioning hybrid nanometal morphing structure.

In Chapter 3, a proof of concept design is selected, in this case a quadrotor propeller blade. The chapter discusses the development of a model to predict aerodynamic behaviour of the propeller blade, and verifies it against the tabulated behaviour of an existing propeller. An optimal twist angle profile is generated through a gradient based optimization.

Chapter 4 uses the generated twist angle profile in order to create, explore, and discuss three different designs that would allow for morphing to occur. These designs are ultimately the hybrid nanometal morphing structure that is desired. Rough models are created for each design, and the morphing mechanisms are examined.

A finite element analysis is performed in Chapter 5 for one of the designs. A full model of the selected design is created for the analysis. A single section of the model is analyzed to give an understanding of the forces required by the actuator, to allow for a mesh convergence analysis to be performed, to verify that the expected shape change from the actuation will occur, and to ensure that the desired magnitude of the change in twist angle will be achieved. This knowledge is then be brought forward for an analysis on the full propeller blade model. Another finite element analysis is performed on this model to verify it can adequately morph while not failing structurally.

Chapter 6 concludes the thesis and gives recommendations for future work involving this hybrid nanometal morphing structure.

Chapter 2

Literature Review

Since aircraft cannot always operate at a single overall optimal design point, there will be room for improvement in its overall efficiency. Morphing can potentially allow for multiple points of optimal flight conditions for an aircraft while it is in flight. For civil aircraft, which can easily have lifespans of 25 years or more, these increased efficiencies can add up to incredible fuel savings, and thus, a significant reduction in emissions.

Implementing morphing in aircraft is not a new concept, and in fact dates all the way back to the Wright Flyer in 1903. This aircraft employed a variable twist wing through the use of cables controlled directly by the pilot in order to control roll [3]. As the demand for structural requirements increased due to higher cruise speeds and weight needs, aircraft structures became more rigid. This made it more difficult to implement a morphing design, as penalties would be imposed upon the aircraft as a result. These penalties are mainly added cost, weight, and complexity of design. However, a morphing design would still be worth implementing as long as the added benefits outweigh the aforementioned penalties.

Figure 2.1 shows a high level overview of various aircraft and their modes of morphing over the years, up until 2010. Early morphing designs and concepts typically consisted of large mechanical systems which impose a relatively high weight penalty, such as a variable sweep wing. This was in a period where reducing emissions wasn't as high a priority as it is now. Due to a greater need for these reductions, morphing designs in aircraft require more benefit from their addition, and less penalties in order to be commercially viable. Technological advancements in materials, structures, morphing, and actuation can make this possible. The following sections will describe some of these advancements, as well as the necessary information and previous work that has been done.

2.1 Early Morphing Designs

The first aircraft to implement a variable sweep wing was the Westland-Hill Pterodactyl IV in 1931. It was actuated by a worm-and-wheel device across the top of the cabin where the front spar would normally have been [24]. This allowed the aircraft to change the sweep of its wings during flight, controlled by either the pilot or the port-side passenger. Also in 1931 was another novel morphing concept, implemented in the Makhonine Mak-10, which sported the first variable span wing. It employed a rail system which would allow the outer panels of the wing to retract into the central ones, allowing the span to increase by 8 m [13]. Later, in 1937 Bakshaev Lig-7 was developed, which featured the first instance of variable chord

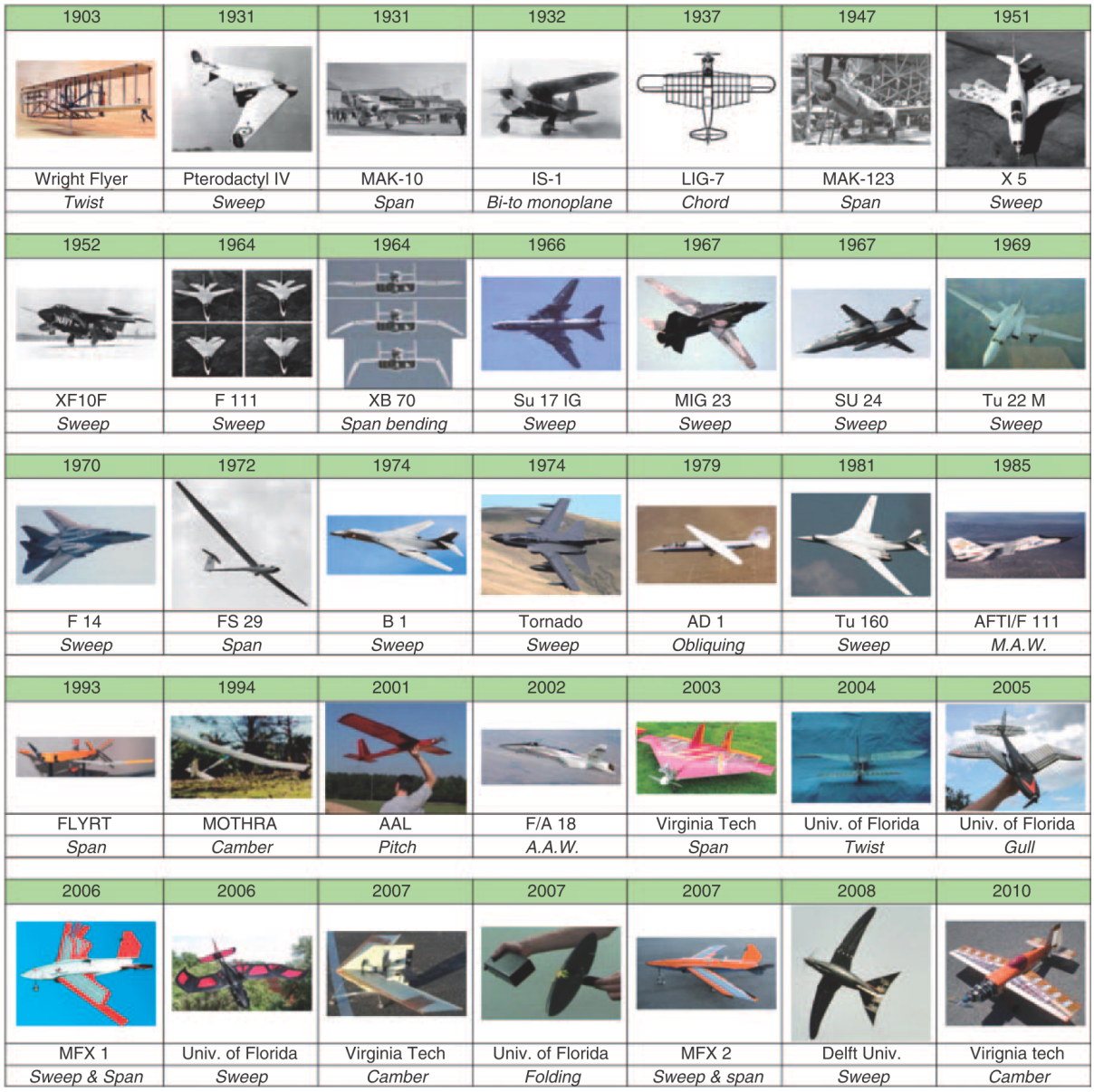

Figure 2.1: Overview of morphing designs in aircraft [3]

morphing capabilities. It was designed with a high aspect ratio, thin wing, which had six individual sections along the span of each wing that could telescope in order to increase the chord [31]. These morphing designs are considered to be large shape changes, and typically induce the penalties discussed earlier to the extent where they may not be viable in terms of net gain to implement.

A trend in morphing research is gearing towards smaller shape changes which don't rely on heavy mechanical systems to implement morphing. These systems also tend to be embedded within the structure they are morphing, and can be capable of changing in response to varying aerodynamic loads. An added benefit of embedded systems is that it allows the structure to maintain a continuous surface, where otherwise a non-continuous surface will likely cause aerodynamic inefficiencies and reduce the effectiveness of a morphing system. One of the first aircraft to implement a small shape change within

an embedded system was the ATFI/F-111 with what is known as a mission adaptive wing. This wing featured an internal mechanism to flex the outer wing skin in order to change the camber of the wing. This allowed for the wing to produce a high camber section for subsonic speeds, a supercritical section for transonic speeds, and a symmetrical section for supersonic speeds [7]. These small change systems require carefully designed morphing structures.

2.2 Morphing Structures

One way to achieve a morphing structure is by actuating trusses that are designed to allow a desired shape change. Some common truss candidates for morphing applications are the Kagome truss, tetrahedral unit cell trusses, octahedral unit cell trusses, and square pyramid trusses. The Kagome truss is based on the Kagome basket weave pattern, where triangles are arranged around a hexagon [16]. This type of truss has been determined to have an isotropic in-plane stiffness and an optimal weight for a specified strength or stiffness among planar trusses. In addition, the members of this truss can be actuated such that arbitrary in-plane nodal displacements can be attained with minimal elastic energy storage. This is true of both the pin-jointed and welded joint infinite planar Kagome truss [16]. These properties make the Kagome truss an excellent candidate for morphing.

Sofla *et al.* developed a rotational joint to be used for the application of morphing structures, which they named a hexa-pivotal (H-P) joint [28]. This joint was constructed by placing a pin through the common centre of two concentric spherical shell elements (links). This allows the links to rotate with respect to each other without interference, with the pin free to rotate about its own axis. Truss members could then be inserted into holes in each link to form a functioning structure. However, this restricts the range of motion of the H-P joint, as the truss members prevent the links from rotating past a certain point depending on their placement.

Sofla *et al.* then used this H-P joint to create a planar morphing hinged truss (PMHT) [29]. It consisted of 6 tetrahedral unit cells arranged in a hexagon to form a larger cell. 3 linear displacement actuators were used per cell, which was determined by using Maxwell's stability criterion (3 mechanisms per cell), resulting in a high authority structure. A high authority structure is defined as a having the ability to morph into different shapes while subjected to significant loads [4]. The PMHT was formed by arranging the cells into a honeycomb pattern, with the centres of a group of seven cells being vacant, as in Figure 2.2. This allowed for a greater number of degrees of freedom over a PMHT without the vacancies. This structure was able to achieve bending, twisting, and undulation deformations.

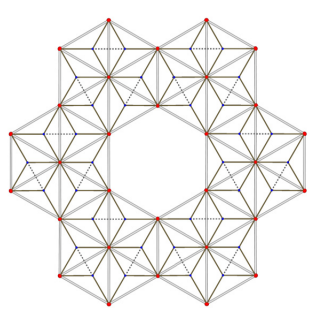

Figure 2.2: Single-layered PMHT with vacancy at the centre

Structures that incorporate these trusses tend to be larger, as manufacturing small unit cells is difficult. This may be an issue depending on the morphing application. Also, the actuators tend to be external to the structure, taking up additional space.

2.3 Compliance and Compliant Mechanisms

Another method to achieve morphing is through the use of compliant mechanisms in a structure. Compliance is the measure of the flexibility of a material, and is the inverse of stiffness. If the flexibility of a material allows it to bend into a configuration that is useful, then it is considered to be a compliant mechanism [14]. There are many types of compliant mechanisms with varying levels of complexity. Three examples are shown in Figure 2.3. Traditionally, structures are designed for strength and stiffness, and, if it is required that parts be capable of motion, joints are introduced in order to facilitate this. Compliant mechanisms are instead designed for strength and compliance. A compliant structure takes advantage of compliant mechanisms in order to achieve motion solely through elastic deformation. As a result, these structures are generally one single part, with no joints or hinges.

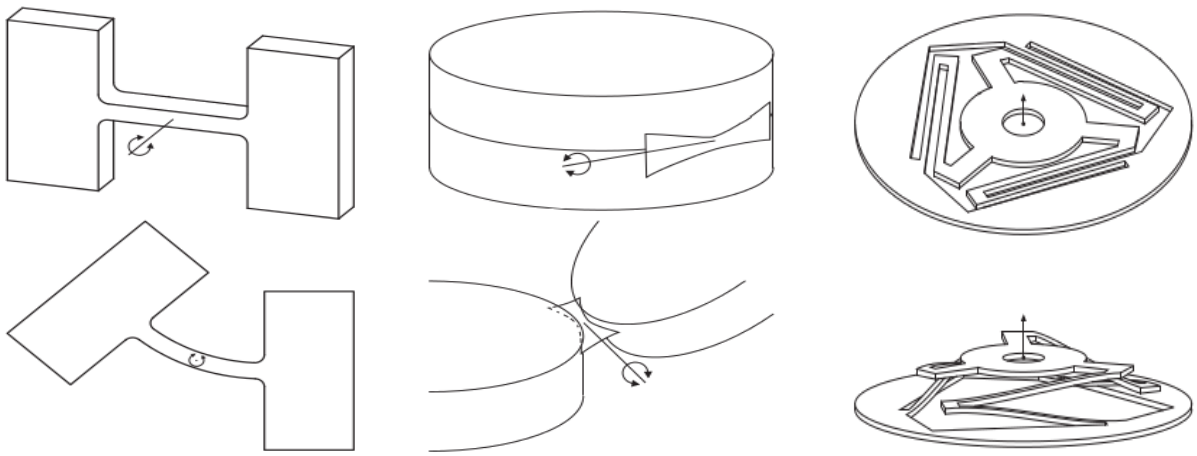

(a) Flexure hinge (b) Bistable hinge (c) Ortho-planar spring

Figure 2.3: Examples of various compliant mechanisms [15]

Since compliant mechanisms have fewer parts, manufacturing costs can be reduced. Also, with no joints, there is less wear on the system and therefore greater reliability. However, there are some tradeoffs in using compliant mechanisms. Fatigue life is of great concern due to the constant loading and unloading of a compliant mechanism. Another complication is maintaining off-axis stiffness, that is, ensuring that the compliant structure does not exhibit motion in an unintended direction. Also, some of the input energy is stored as elastic work in the compliant mechanism, which reduces the efficiency of the system [22].

2.4 Actuators

There are many different types of actuators, each with varying properties. For the purpose of implementation into a morphing structure, some actuators are not practically feasible. From size and weight constraints, pneumatic and hydraulic actuators cannot be considered. This leaves electrical and thermal

actuators to choose from. In these two classes, the most promising options are piezoelectric actuators and shape memory alloys (SMAs). This selection is based on practicality, availability, and capability for embedding. Embedding an actuator within a structure allows for a more compact system overall.

Piezoelectric materials work by voltages inducing lattice displacements. These lattice displacements results in a macroscopic strains. Advantages of piezoelectric actuators include high bandwidth, a high power output per unit volume, and reasonable efficiency [18]. However, piezoelectric actuators have a relatively small blocking force and free stroke. The blocking force is the maximum force the actuator can produce, with zero displacement. The free stroke is the maximum displacement the actuator can achieve under no load. For linear piezoelectric actuators, the blocking force typically ranges from 100 to 4000 N, where the free stroke typically ranges from 10 to 100 μm. A diagram illustrating the operating region of a generic piezoelectric actuator is shown in Figure 2.4. Since the blocking force and free stroke are small, piezoelectric actuators may not be able to produce the required displacements in a structure to achieve the desired morphing. Large displacement piezoelectric actuators have been designed by taking advantage of mechanisms such as a bridge-type mechanical amplifier [19]. However, these amplified piezoelectric actuators are generally large, and produce displacements perpendicular to the axis of the largest dimension. As a result, implementation into a tube-like structure will not be possible. These factors reduce the viability of using piezoelectric actuators for the purpose of morphing in a compliant mechanism.

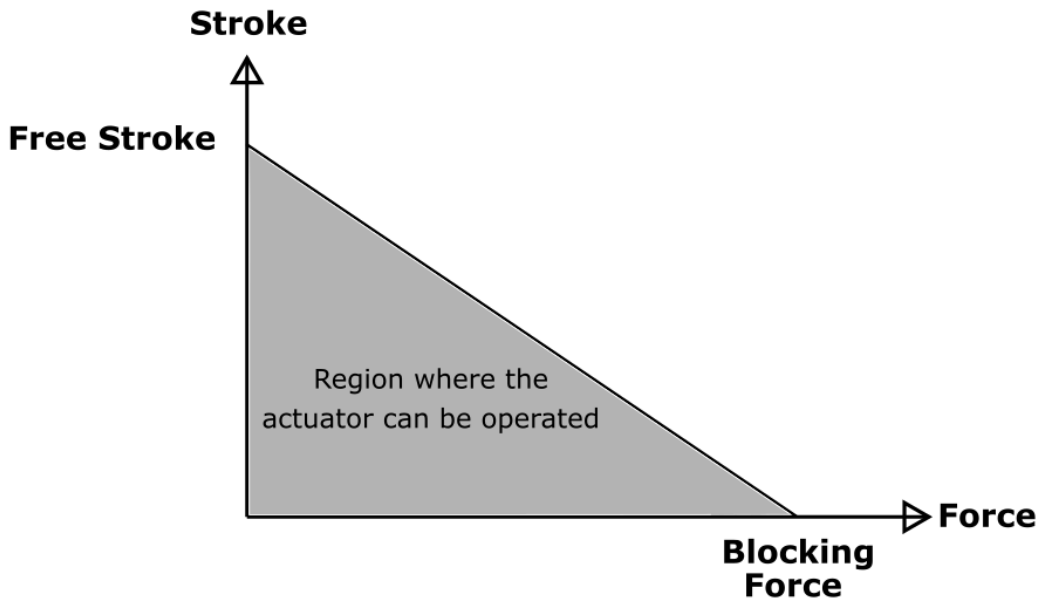

Figure 2.4: Stroke-Force curve for an actuator [25]

SMAs work by way of the shape memory effect. SMAs can exist with two different phases: austenite and martensite. The austenitic phase is stable at higher temperatures, while the martensitic phase is stable at lower temperatures [18]. Different geometric shapes can be associated with the different phases so that raising or lowering the temperature past the activation temperature will induce a macroscopic change in configuration. Heating a thermally activated SMA induces this phase change, and thus shape change. There exist two types of SMAs: one-way and two-way. One-way SMAs change shape when heated, but returning to the "cold temperature" shape requires an external load. Two-way SMAs can

return to the "cold temperature" shape by reducing the temperature, which reverses the phase change. While two-way SMAs seem more useful, it comes at a price. Two-way SMAs cannot recover as much strain as one-way SMAs, and the strain tends to deteriorate more quickly [27]. Two-way SMAs require a training process in order to achieve the desired shapes. The SMA is subjected to a high temperature (between $400 - 500°C$) under an applied force for 30 minutes at the desired "hot temperature" shape. Afterwards, the SMA is reshaped to its "cold temperature" shape and rapidly quenched [8]. The SMA can be refined further through thermomechanical training which applies a constant stress and cycles the temperature through the SMA's activation temperature. This provides enhanced stress and strain properties at the cost of some irrecoverable deformation [23].

In general, SMAs have a very high work density, are able to achieve up to 10% strain and are able to exert large forces. However, they have low energy efficiencies, low actuation frequencies, and small bandwidth [18]. These drawbacks may not be very problematic in an aerospace application. If the frequency of actuation required is in the range of the capability of the actuator, or less, then the only major issue with implementing an SMA is the low energy efficiency. Therefore, the effectiveness of implementation depends heavily on the nature of the required application.

2.5 Nanometal Hybrid Structures

Hybrid nanocrystalline structures are a relatively new technology that was developed at the University of Toronto and Integran Technologies Inc. in 2008, through the electrodeposition of nanocrystalline nickel onto a 3D printed polymer substrate [12]. Because of the Hall-Petch effect, the strength of a material increases as the grain size decreases. Therefore, all things held equal, nanocrystalline nickel will be stronger than polycrystalline nickel. However, working a material that has undergone this process into a useful geometry becomes significantly more difficult as a result. Electrodeposition onto a polymer substrate allows for complex geometries to be created with a material having its grain size of 10-100 nm.

There are two classes of these nanocrystalline microtrusses: polymer or metal cores. The electrodeposition process is the same for both, but the manufacturing of the core is different. The polymer core can be created very easily using a standard 3-D printer. As a result, very complex structures may be created by relatively simple means. For the metal core, there are different processes that can be used. One process is to create a sheet of the metal with the geometry of the struts and nodes projected onto this sheet. Pins are then used to hold some of the nodes in place, while appyling a force to the other nodes in a heated environment in order to achieve the final truss core. As a result, it is more difficult to create complex geometries than with the polymer substrate. This applies to the other methods as well. Since nearly all of the structural strength is from the coating, the core only contributes mass to the structure, which is undesirable [21]. In this work, only the polymer substrate will be considered.

The electrodeposition process allows for a material to be plated with a thin layer of nanocrystalline nickel, iron, or cobalt, or an alloy of these metals. For nickel, this is accomplished by placing the material in a bath of nickel sulfate, nickel chloride, boric acid, grain size inhibitors, grain nucleators, and stress relievers [10]. This bath must be both temperature and pH controlled in order to achieve the desired results. An anode, preferably an electrolytic nickel anode, is connected to a DC power source, as well as a cathode (preferrably titanium). The current is pulsed on and off for very short times - typically 1.0 to 5.0 ms on and between 30 and 50 ms off. This facilitates the actual electrodeposition of the selected metal onto the material. As a result of this process, nanocrystalline nickel with grain sizes as low as

10 nm has been successfully electrodeposited onto various materials.

The reason this technology is so attractive to aerospace applications is that very strong structures may be created with complex geometries that would be very costly or impossible to manufacture. The material produced has a very similar strength-to-weight ratio as regular nanocrystalline nickel while being significantly less dense than its counterpart. The reduced density is due to using a hollow structure combined with the polymer substrate. It also allows for actuators to be embedded within the structure. This would lead to a much more compact structure, opening up morphing structures to more potential applications where compactness is a necessity.

Chapter 3

Aerodynamic Optimization

During the course of exploring morphing structures and their applications, it was decided that a proof of concept implementation would be valuable in proving the value of the combined technologies explored in Chapter 2. Specifically, this would be combining nanometal hybrid structures with actuators in a morphing structure, and potentially a morphing skin in order to create a part that would be more efficient overall to its non-morphing counterpart. The application that was selected was morphing propeller blade for a quadrotor. It was observed that these propeller blades are not typically designed for a specific application, rather, one is chosen that would best suit the situation. It was felt that designing a morphing propeller blade for a specific application could provide significant efficiency improvements as a result.

In order to design this propeller, an aerodynamic optimization is necessary. This would require two aerodynamic frameworks that would capture various aspects of flow around the propeller so that an optimal structure could be determined. The frameworks needed are blade element momentum theory, the vortex panel method, and an optimization algorithm.

3.1 Blade Element Momentum Theory

Blade element theory is used to determine the performance of propellers. This is done by dividing a blade into elements and applying force and moment balances on each individual element in 2D space [11]. For a given element, the thrust, T, is

$$\mathrm{d}T = \mathrm{d}L\cos(\phi) - \mathrm{d}D\sin(\phi), \tag{3.1}$$

where L is lift, D is drag, and ϕ is the difference between the pitch angle, θ and the angle of attack, α. Similarly, the torque, Q, is given as

$$\frac{\mathrm{d}Q}{r} = \mathrm{d}D\cos(\phi) + \mathrm{d}L\sin(\phi), \tag{3.2}$$

where r is radius at the beginning of the current element of the propeller blade. The expressions for lift and drag, approximating the blade elements as rectangular, are

$$\mathrm{d}L = \frac{1}{2}C_L\rho V^2 c_i \mathrm{d}r; \tag{3.3}$$

$$\mathrm{d}D = \frac{1}{2} C_D \rho V^2 c_i \mathrm{d}r. \tag{3.4}$$

We can then substitute equations 3.3 and 3.4 into 3.1 and 3.2, yielding

$$\mathrm{d}T = \frac{1}{2} \rho V^2 c_i (C_L \cos(\phi) - C_D \sin(\phi)) \mathrm{d}r; \tag{3.5}$$

$$\mathrm{d}Q = \frac{1}{2} \rho V^2 c_i (C_L \sin(\phi) + C_D \cos(\phi)) r \mathrm{d}r. \tag{3.6}$$

For a given lift and drag coefficient, equations 3.5 and 3.6 can be numerically summed to determine the thrust and drag acting on each blade. These values are multiplied by the total number of blades in order to determine the thrust and torque from the propeller as a whole. Further detail on the determination of the lift and drag coefficients will be discussed in Section 3.2

Next, the inflow effects for the propeller need to be taken into account. For the axial flow, the velocity change can be approximated by an increase by a factor of c_1 with respect to the quadrotor forward velocity, V_f. This can be represented by

$$V_1 = V_f(1 + c_1). \tag{3.7}$$

For the angular flow, the velocity change can again be approximated by a reduction by a factor of c_2 with respect to the tangential velocity of the propeller blade.

$$V_2 = \Omega r(1 - c_2), \tag{3.8}$$

where Ω is the angular velocity of the propeller in rad/s. We can now calculate the magnitude of the velocity vector of the flow,

$$V = \sqrt{V_1^2 + V_2^2}, \tag{3.9}$$

as well as the angle of attack

$$\alpha = \theta - \tan^{-1}(\frac{V_1}{V_2}). \tag{3.10}$$

To calculate the values of c_1 and c_2, we need to apply conservation of momentum to the flow in both the axial direction. Assuming steady flow,

$$\begin{aligned} \mathrm{d}T &= \mathrm{d}\dot{p} \\ &= \dot{m}\mathrm{d}V \\ &= \rho 2\pi r V_1 (V_s - V_f)\mathrm{d}r, \end{aligned} \tag{3.11}$$

where V_s is the slipstream velocity. Figure 3.1 illustrates the various velocities with respect to the propeller. Assuming the axial velocity in the plane of the propeller is the average of the slipstream velocity and the inflow velocity (forward velocity) in combination with equation 3.7, we have

$$\begin{aligned} V_1 &= \frac{1}{2}(V_s + V_f) \\ V_s &= V_f(1 + 2c_1). \end{aligned} \tag{3.12}$$

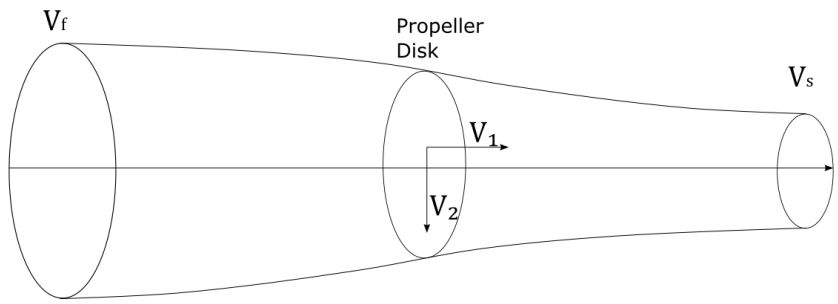

Figure 3.1: Visualization of velocities for blade element momentum theory

Substituting this into equation 3.11, we obtain

$$\begin{aligned} \mathrm{d}T &= \rho V_f(1+a)2\pi r\mathrm{d}r(V_f(1+2c_1)-V_f) \\ &= \rho 4\pi r V_f^2(1+c_1)c_1\mathrm{d}r. \end{aligned} \tag{3.13}$$

Similarly, applying the conservation of angular momentum in the same plane,

$$\begin{aligned} \mathrm{d}Q &= \mathrm{d}\dot{L}r \\ &= \dot{m}\mathrm{d}Vr \\ &= \rho 2\pi r^2 V_1 V_\theta \mathrm{d}r. \end{aligned} \tag{3.14}$$

If we assume that the tangential velocity is twice the value of the reduction in tangential velocity due to inflow effects

$$V_\theta = 2c_2\Omega r, \tag{3.15}$$

substituting equations 3.15 and 3.7 into 3.14, we have

$$\begin{aligned} \mathrm{d}Q &= \rho 2\pi r^2 V_f(1+c_1)2c_2\Omega r\mathrm{d}r \\ &= \rho 4\pi r^3 V_f(1+c_1)c_2\Omega\mathrm{d}r. \end{aligned} \tag{3.16}$$

We can now use equations 3.5, 3.6, 3.9, 3.10, 3.13, and 3.16 to formulate an iterative solution.

3.1.1 Inclusion of Motor and Weight

At this point, the thrust and torque generated from a propeller for a given geometry, forward velocity, and an assumed RPM can be determined. However, the operating RPM will depend on the performance characteristics of a motor chosen for the propeller alongside the aerodynamic conditions. For a specified motor, the torque from the propeller can be used in conjunction with the motor equations to determine the new RPM value. This can be done iteratively with the blade element momentum theory framework until the assumed RPM converges with the operating RPM. The motor equations are

$$\Omega = K_v(v - ir_M), \tag{3.17}$$

$$Q = \frac{i - i_0}{K_v}, \tag{3.18}$$

where K_v is a motor constant, i_0 is the no-load current at a specific voltage, and r_M is the internal resistance of the armature. Equation 3.18 can be substituted into 3.17 to yield

$$\Omega = K_v(v - (K_v Q + i_0)r_M). \tag{3.19}$$

Now that the solution to the thrust produced is known and has completely converged, some checks are required in order to make sure that the quadrotor will actually fly. First, it needs to be ensured that the motor can achieve the RPM that was determined by checking the manufacturer's specifications. Second, the power required by each propeller needs to be checked such that it can be supplied by the chosen motor. If either of requirements these fail to pass the check, a more powerful motor needs to be selected. Third, using the assumed overall weight of the quadrotor, the minimum thrust required for level flight can be determined and the thrust from the four propellers can be checked to see if it exceeds this value. If it does not, a propeller that produces more thrust needs to be selected, or the quadrotor needs to fly at a different speed.

3.1.2 Assumptions

It was assumed that the quadrotor will only experience forward, level flight, or be hovering. As a result, no elevation changes occur, and the density and viscosity of air remain constant. When applying conservation of momentum, it is assumed that the flow is steady. This is not applicable to a turbulent flow, which may result in some errors in determining the flow velocities.

In order to determine the minimum thrust required, the weight of the quadrotor was assumed. This was based of other current quadrotor design specifications. The effect of the quadrotor's body was neglected, meaning no additional drag forces are produced. This may cause problems if the total thrust produced is close to the thrust required to maintain level flight.

3.2 Vortex Panel Method

One method that can determine the lift and drag coefficients for a flow around an airfoil is the vortex panel method. This method can be applied to an airfoil of arbitrary thickness and camber, with the numerical solution agreeing well with the analytical [20]. It calculates the velocity and pressure distribution around the entire airfoil, and from this, the lift and drag can be determined.

This method requires the input of an angle of attack for the airfoil as well as a detailed geometry of the airfoil. It starts by breaking down the airfoil into discrete vortex panels of linearly varying strength in a clockwise direction starting from the trailing edge. Control points are placed at the middle of each panel, and the lengths and orientation angles of each panel are calculated. The orientation angle is determined from the x-axis to the surface of the panel. This can be seen in Figure 3.2. The velocity potential η at the ith control point in a uniform flow V_∞ at angle of attack α and m vortex panels can be written as

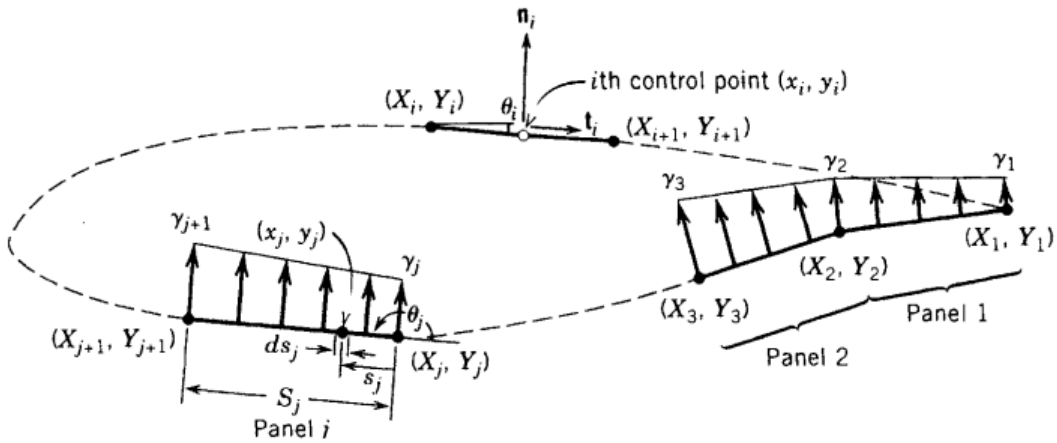

Figure 3.2: Illustration of the vortex panel method on an airfoil [20]

$$\eta(x_i, y_i) = V_\infty(x_i \cos\alpha + y_i \sin\alpha) - \sum_{j=1}^{m} \int_j \frac{\gamma(s_j)}{2\pi} \tan^{-1}(\frac{y_i - y_j}{x_i - x_j}) \mathrm{d}s_j. \tag{3.20}$$

where

$$\gamma(s_j) = \gamma_j + (\gamma_{j+1} - \gamma_j)\frac{s_j}{S_j}, \tag{3.21}$$

γ_j being the circulation density of the jth panel of length S_j at a distance of s_j from the leading edge of the panel. Next, the circulation density associated with each panel needs to be calculated. The velocity normal to each panel is zero at each control point according to the imposed boundary condition, noted as

$$\frac{\partial}{\partial n_i}\eta(x_i, y_i) = 0; \qquad i = 1, 2, ..., m. \tag{3.22}$$

The resulting differentiation and integration of the combinations of equations 3.22 and 3.20 will result in the following expression

$$\sum_{j=1}^{m}(C_{n1_{ij}}\gamma'_j + C_{n2_{ij}}\gamma'_{j+1}) = \sin(\theta_i - \alpha); \qquad i = 1, 2, ..., m, \tag{3.23}$$

where $\gamma' = \gamma/2\pi V_\infty$ is the non-dimensional circulation density of the jth panel, θ_i is the orientation angle of the ith control point, and $C_{n1_{ij}}$ and $C_{n2_{ij}}$ are normal-velocity influence coefficients. These coefficient are explicitly calculated using panel sizes, orientations, and control point locations on the panels. Next, the Kutta condition needs to be imposed on the trailing edge to ensure smooth flow. This is represented as

$$\gamma'_1 + \gamma'_{m+1} = 0, \tag{3.24}$$

combining equations 3.23 and 3.24 results in $m+1$ equations and unknowns, meaning the linear system can be solved. The non-dimensional circulation densities can then be determined for each panel. A

similar expression to equation 3.23 one can be obtained in the tangential direction, but with non-zero velocities

$$V_i = \cos(\theta_i - \alpha) + \sum_{j=1}^{m}(C_{t1_{ij}}\gamma'_j + C_{t2_{ij}}\gamma'_{j+1}); \qquad i = 1, 2, ..., m, \tag{3.25}$$

where V_i is the local dimensionless velocity and $C_{t1_{ij}}$ and $C_{t2_{ij}}$ are the tangential-velocity influence coefficient and calculated similar to $C_{n1_{ij}}$ and $C_{n2_{ij}}$. With the circulation densities, the non-dimensional local velocities can be computed at each control point using equation 3.25, and thus the coefficient of pressure at each control point using

$$C_{p_i} = 1 - V_i^2. \tag{3.26}$$

The coefficients of lift and drag can be determined through the numerical integration of the calculated pressure coefficients over each panel.

The combination of the vortex panel method with blade element momentum theory can allow for a more detailed and accurate analysis of the forces acting upon the overall propeller. This will be useful when designing an underlying structure for a propeller.

3.3 Optimization Algorithm

The algorithm implemented is a gradient descent optimization for the maximization of lift experienced by the propeller by determining the optimal twist angle for the sections across the length of the propeller. This was re-framed as a minimization of the inverse of lift. The algorithm begins by calculating the coefficient of lift as per the vortex panel method described in Section 3.2 at the current conditions assumed. It then calculates another coefficient of lift at a small change to the twist angle of each section of the propeller independently of each other. These coefficients are then converted from their non-dimensional form using

$$L = \frac{1}{2}C_L\rho v^2 s. \tag{3.27}$$

The gradient is calculated using a first order finite difference. The step size for the change in twist angles is calculated using a backtracking line search. This method was used in order to ensure descent towards the optimal point. The twist angles are then updated by the determined amount. This process is repeated until convergence within the tolerance level chosen.

3.4 Assigned Conditions and Properties

In order for morphing to be able to occur within the propeller structure, two distinct geometries must be generated by the algorithm. To achieve this, 2 sufficiently different aerodynamic conditions must be chosen, but also be realistic in terms of performance for the overall drone. As a result, the two aerodynamic conditions chosen were hover and a forward flight with a velocity of 15 m/s. The algorithms in Sections 3.1 - 3.3 are not capable of generating a propeller geometry from scratch, only optimizing an existing one. Thus, a starting propeller geometry needed to be chosen.

For the initial airfoil profile, a NACA 2412 was selected for the entire length of the propeller, as shown in Figure 3.3. This was chosen because of its readily available airfoil geometry and non-symmetrical profile. It was discretized into 16 sections, with chord properties assigned based on the APC thin electric 9x6 propeller [6], and thickness properties determined from the NACA 2412 airfoil that was selected. This also resulted in choosing a length for each propeller of nine inches, with two blades per propeller. These propeller properties were also chosen due to its readily available geometry as well as other data and visualizations provided as reference and context. A twist angle of 10° was assigned to each discrete propeller section as an initiation point for the optimization. Next, the motor was selected based on these initial, assumed conditions being implemented into the blade element momentum and vortex panel method portions of the algorithm, independent of the optimization. This was to get a general sense of the performance characteristics in addition to determining the general requirements of what would be the resulting quadrotor. The AXI 2814/10 Gold Line V2 motor was selected based on the outputs generated [1]. A battery with 5000 mA-h of charge was selected to power each motor. It should be noted that there would be one battery per motor per propeller, for a total of four of each. The mass was also determined based on the motors, some additional amount for the batteries as well as an assumed amount for the remaining quadrotor body, totaling 3.6 kg overall. This also assumes no payload for the quadrotor. Standard air density and viscosity was assumed, as well as a freestream velocity of 5 m/s for the air conditions. Lastly, the error threshold was chosen to be 1×10^{-6}.

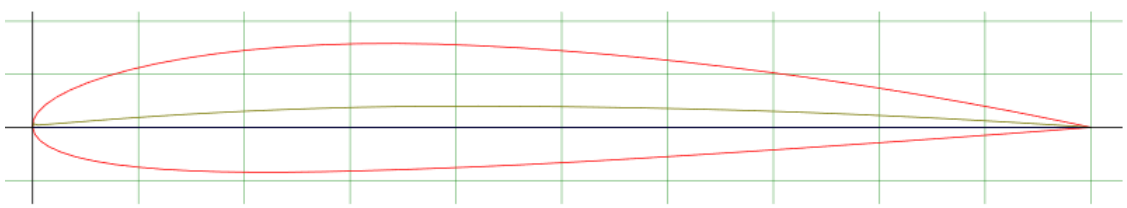

Figure 3.3: NACA 2412 airfoil

3.5 Optimization Results

After running the algorithm with the values assigned from Section 3.4 for both the hover and forward flight conditions, two optimized profiles for the twist angle were generated. The exact values can be seen in Table 3.1. The absolute difference and percent change in the twist angle was determined and is shown in Table 3.2. The optimized hover condition propeller configuration provides a 14.49% increase in lift over the NACA 2412 airfoil at a 0° twist angle, while the optimized forward flight condition configuration provides an increase of 10.48%. A curve was fit to the profiles generated and was plotted, as seen in Figure 3.4. It should be noted that the discretization begins at an r/R value of 0.1. This is due to the fact that the root of the blade needs to be attached to the hub, which in this case is assumed to have a 0.9 inch radius. The twist angle appears to reach quite high values, but these are not unrealistic. The profiles seem to follow similar patterns for existing propellers after employing an eye test in order to verify the results in a qualitative manner.

The pressure distribution for the NACA 2412 airfoil from the vortex panel method was plotted and compared to the XFOIL output as a quantitative validation, using an angle of attack of 5.5°. The results can be seen in Figure 3.5 and Figure 3.6. The optimized twist angles were then applied to the

base geometry of the NACA 2412 airfoil selected at the discretized sections selected, along with the chord values assigned in order to generate unprocessed profiles along the length of the optimized propeller. This can be seen in Figure 3.7. These geometries can then be inputted into the code comprising solely of the blade element momentum theory and the vortex panel method in order to determine the exact operating parameters and forces generated as well as acting upon the propeller blades. The determined parameters can be seen in Table 3.3. The lift profiles generated were plotted and can be seen in Figure 3.8. All of the generated and outputted operating conditions and parameters were compared quantitatively to those of tabulated values for existing propellers, and they all seem to be in the realm of realism and normalcy.

r/R	Hovering (°)	Forward Flight (°)
0.10	30.26	31.41
0.16	31.17	33.27
0.22	31.81	33.98
0.28	55.98	65.59
0.34	61.31	66.85
0.40	60.41	64.38
0.46	58.34	62.25
0.52	54.61	58.11
0.58	43.53	45.73
0.64	38.76	40.56
0.70	33.12	34.48
0.76	29.13	30.20
0.82	24.74	25.51
0.88	21.82	22.42
0.94	18.39	18.79
1.00	15.09	15.32

Table 3.1: Twist angle results at discrete sections of the propeller

r/R	Absolute difference (°)	Percent change (%)
0.10	1.15	3.80
0.16	2.10	6.73
0.22	2.17	6.80
0.28	9.61	17.16
0.34	5.54	9.05
0.40	3.97	6.16
0.46	3.41	6.27
0.52	3.50	6.04
0.58	2.20	4.80
0.64	1.80	4.44
0.70	1.34	3.93
0.76	1.07	3.56
0.82	0.77	3.05
0.88	0.60	2.68
0.94	0.40	2.14
1.00	0.23	1.48

Table 3.2: Twist angle difference between hovering and forward flight

With confidence about the optimization results, the next step is to process the generated twist

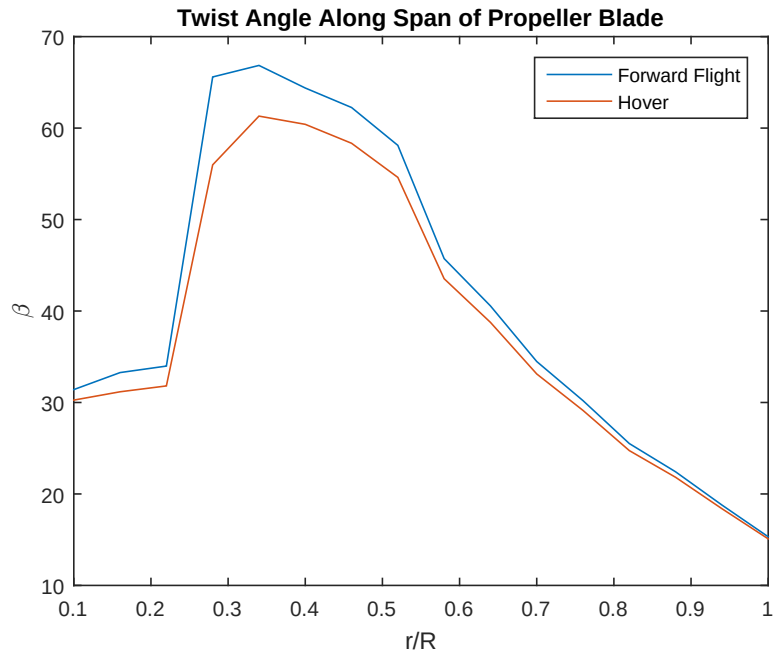

Figure 3.4: Optimized twist angle profiles

	Velocity (m/s)	RPM	Torque (N·m)	Thrust (g)
Hovering	0	14347	0.0825	1430
Forward Flight	15	14697	0.143	1936

Table 3.3: Operating parameters at specified flight condition

distribution into a design capable of morphing from one to the other and back. This will require exploring various design concepts and implementations.

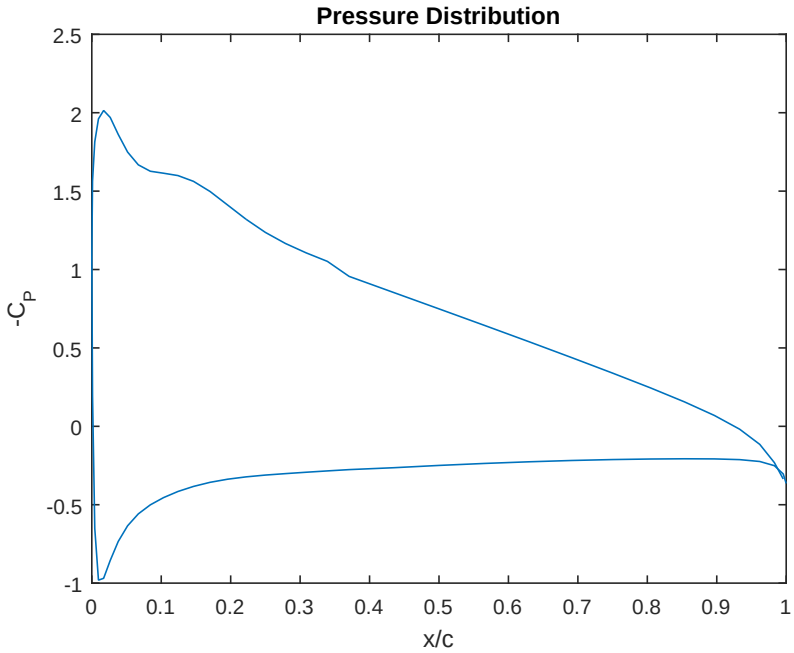

Figure 3.5: Calculated pressure distribution of NACA 2412 airfoil at $\alpha = 5.5°$

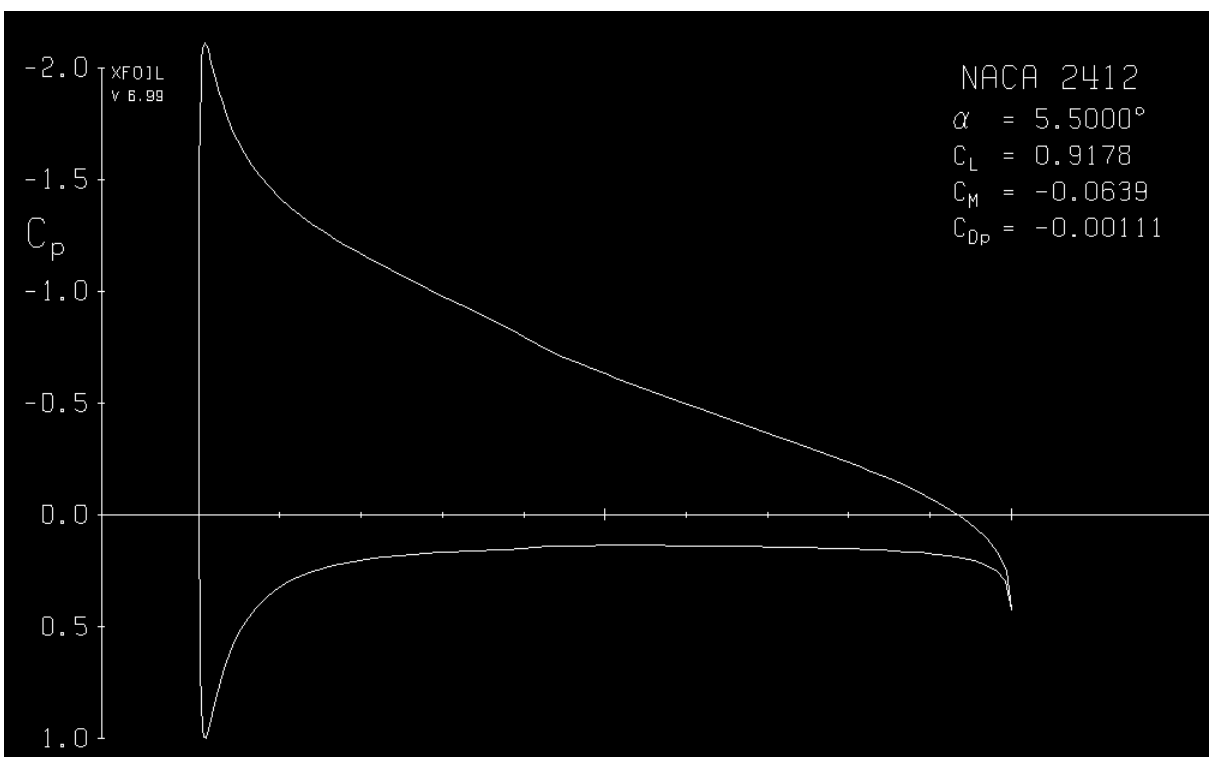

Figure 3.6: XFOIL pressure distribution of NACA 2412 airfoil at $\alpha = 5.5°$

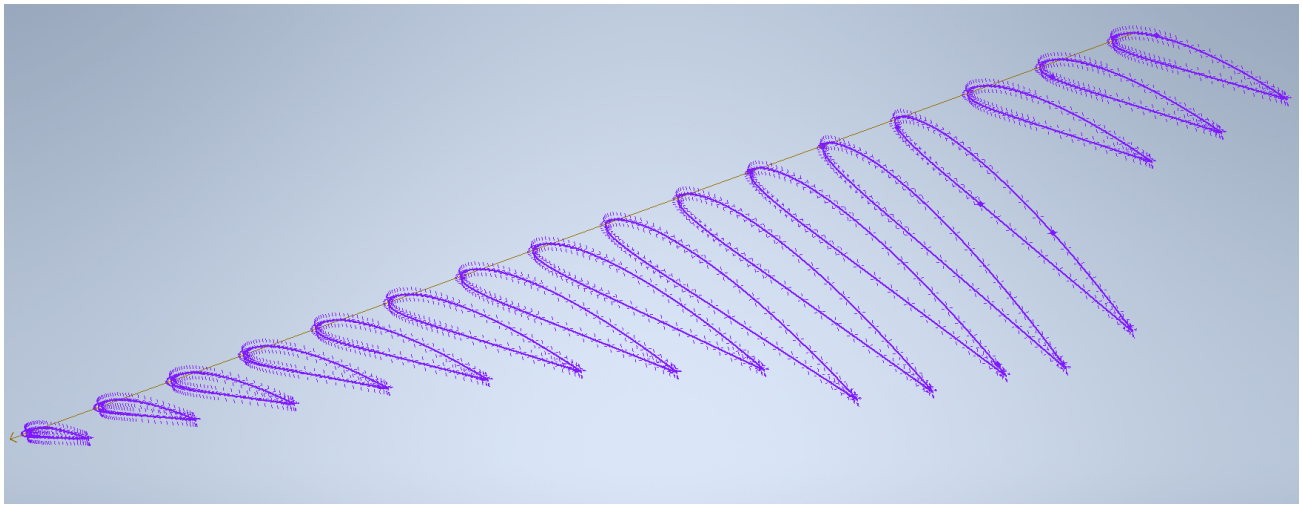

Figure 3.7: Propeller profiles generated at discrete sections

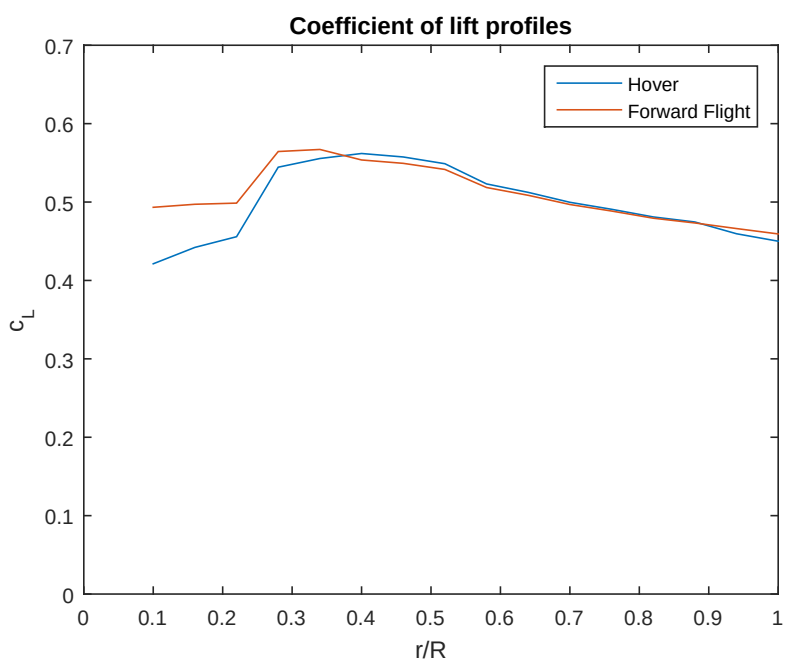

Figure 3.8: Lift distribution across propeller span

Chapter 4

Design Concepts

In this chapter, various designs will be conceptualized and subsequently developed in order to make them as efficient and viable as possible, while being sufficiently different. This is done to give an idea of the design process and various considerations that need to be taken into account. In Chapter 3, an optimal geometry profile was determined, from calculated optimum twist angles. Certain assumptions were made however, such as an overall mass. This should to be taken into account during the design process, as the performance of the propeller can be improved.

All of the designs explored have commonalities. The first is that each design needs to be capable of changing the shape of the airfoil profiles generated in Chapter 3 from one to the other and back. This will require some form of actuation, meaning the inclusion of actuators in the structure. These actuators need to be powered, requiring some sort of electrical connection from a power source. The power source will not be within the scope of the designs, however the inclusion of the electrical connections will be. Next is that each design will have a polymer substrate with a nanometal coating electrodeposited onto it. Each design will need to be capable of being 3D printed and subsequently electrodeposited. Last, the structures need to be able to withstand the forces acting upon them so they do not fail.

An important note is the fact that some of the twist angle changes determined in the Chapter 3 are relatively small in magnitude. While inducing morphing for the twist angles upon changing the flight regime for a quadrotor would require all of the sections to change in order to achieve its optimal performance, it may not be economically worth actuating certain sections. That is to say, the voltage spent on actuating sections with small changes in twist angle may not in fact increase the performance of the quadrotor enough to do so. Also, for designs with connections between each discrete section, forces would propogate along the span of the propeller so that actuating one section will have an effect on the change in the twist angle in the subsequent sections. This could potentially reduce the overall actuation force required from the actuators for the overall structure versus the sum of actuating the individual sections if they were to be isolated. Similarly, the connection of the root of the propller blade to the propeller hub would in fact increase the stiffness of the sections close to it, which could result in requiring a higher actuation force in order to achieve the required morphing than if there were no connection.

4.1 Design 1 - Solid Body

The first design concept that will be explored starts with a solid polymer substrate to be coated with a nanometal, with external actuators that will apply forces to change the shape of the propeller blade locally. Images illustrating this concept can be seen in Figures 4.1, 4.2, 4.3, and 4.4.

The idea is that the actuators will be placed at sections, either on top of the blade or underneath and bonded to the blade itself. Upon activation, the actuator will either expand or contract, imparting a force on the blade. This force will cause the section to increase or decrease the local twist angle depending on the actuator's location and the direction of the actuation. The conceptual images show a total of three actuator strips on top and two on the bottom. In these images, the actuators are not placed across the entire span of the propeller, but rather a portion of it. If this design were to be implemented, multiple actuators may need to be placed along the span of the blade in order to achieve the desired shape change.

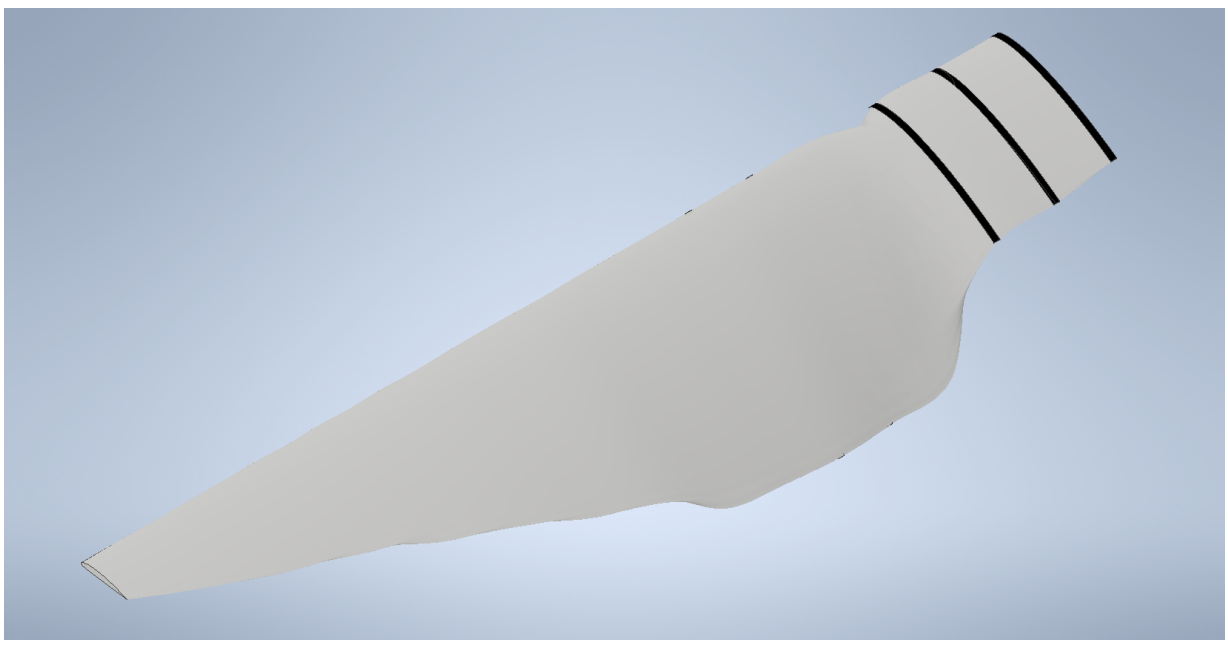

Figure 4.1: Isometric view showing top side of propeller blade with three actuator strips

Since the propeller blade is a solid structure, it would be relatively stiff when compared to a potential cellular solid design using the same materials. In bending applications, the deflection of a point scales linearly with respect to both the Young's modulus and the second moment of area. Since the material will be the same for both, only the second moment of area can be changed to affect this. To reduce the magnitude of force required, the structure could be made to be hollow, reducing its bending stiffness while also reducing the mass of the structure. Although almost all of the stiffness would come from the coating, any decrease translates to a reduction in the actuation force required from the actuators. To illustrate this further, the stiffness of the candidate 3D printing material, VisiJet Crystal, is 1.5 GPa, where the stiffness of the nanometal, nanocrystalline nickel, can be up to 200 GPa. The thickness of the nanometal coating applied to the polymer substrate tends to be on the order of hundreds of microns, so the second moment of area of the coating will be of similar order to the polymer substrate. The

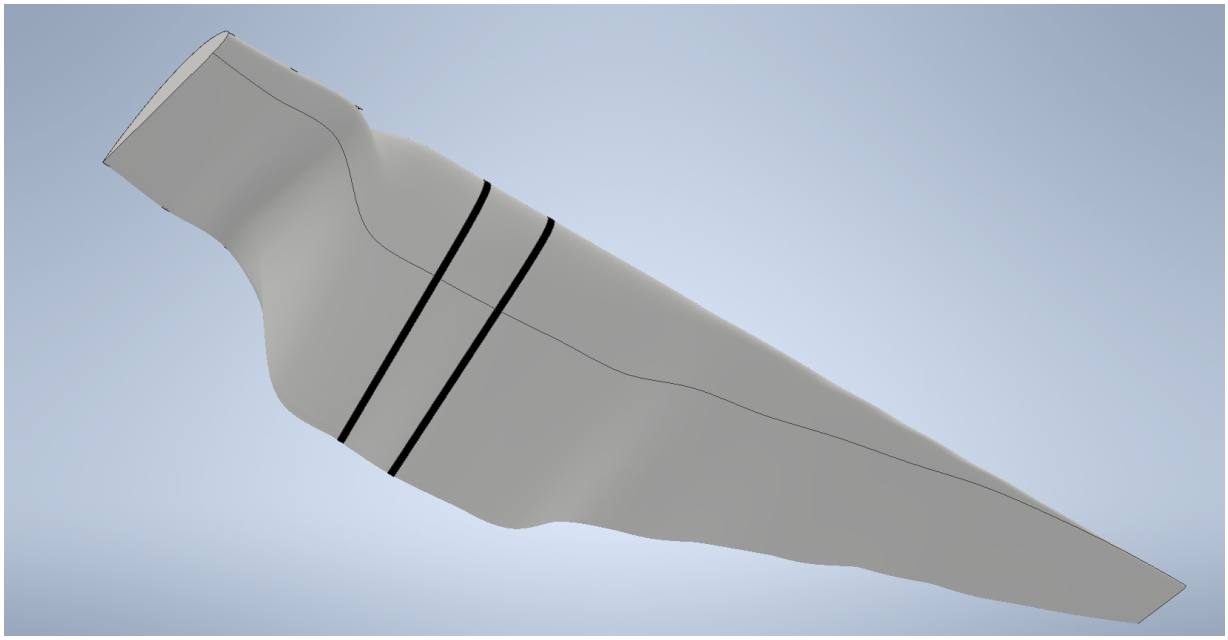

Figure 4.2: Isometric view showing bottom side of propeller blade with two actuator strips

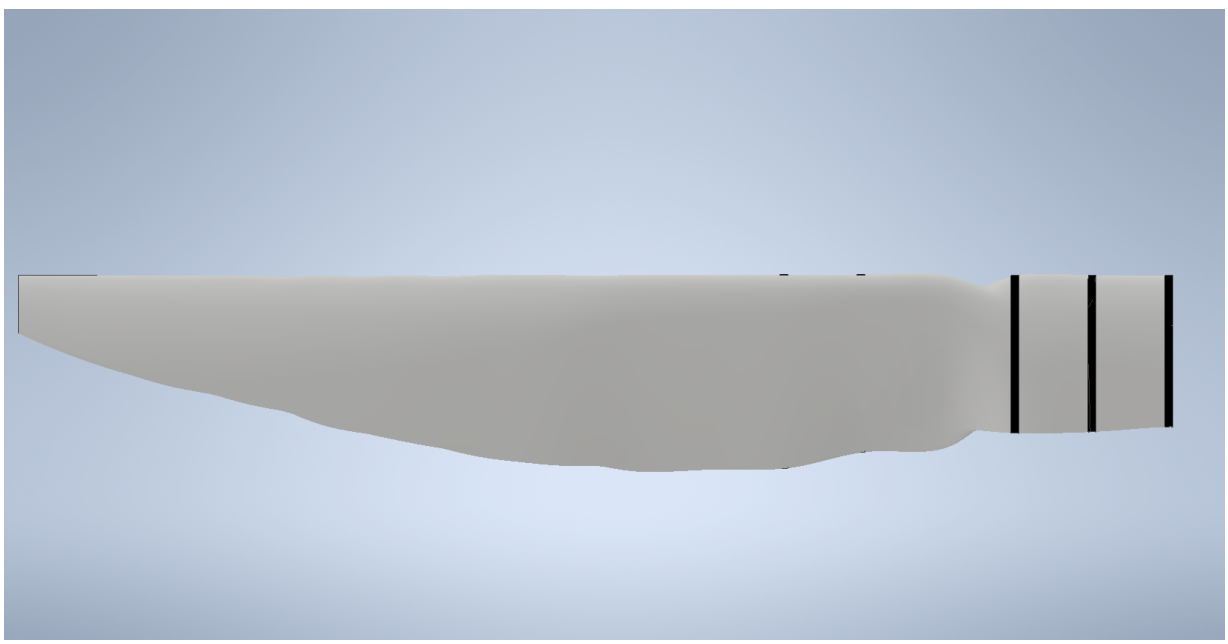

Figure 4.3: Top view of propeller blade with 3 actuator strips

second moment of area is strictly a geometric calculation based on how material is distributed about a two dimensional section's neutral axis. The combination of the thin nanometal coating thickness and the relatively large distance away from the neutral axis will result in a value which is a similar order of magnitude as that of the large thickness of the polymer substrate that is on average much closer to the neutral axis. The bending stiffness is defined as the section's Young's Modulus, E, multiplied by

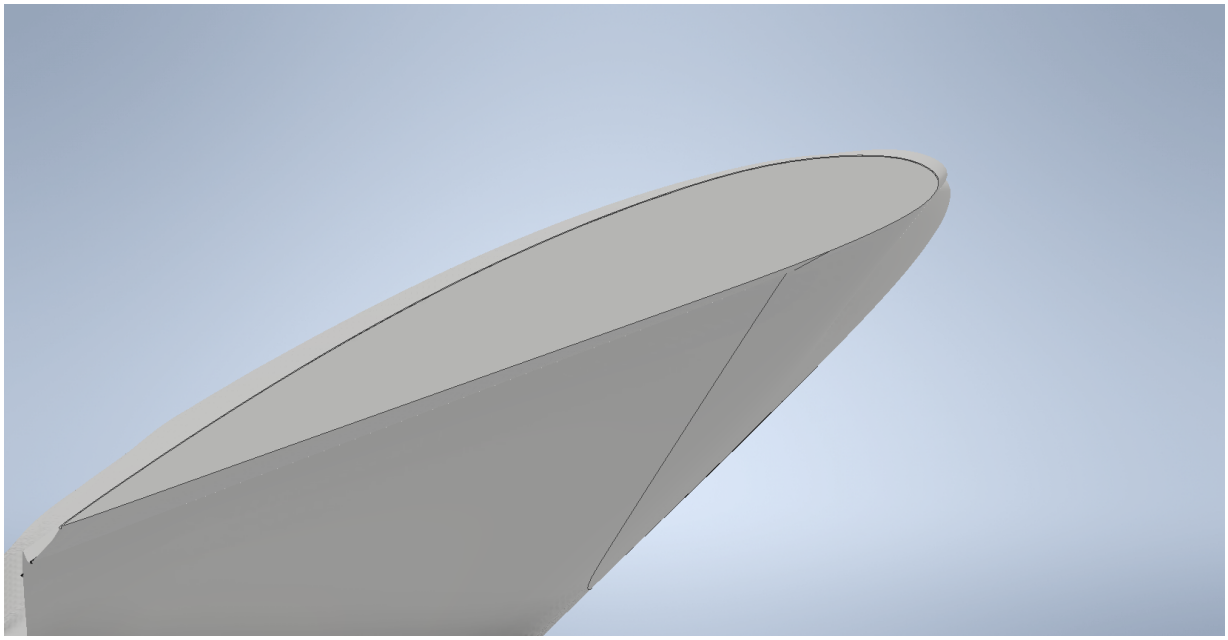

Figure 4.4: Side view at root of propeller blade showcasing a thin strip of an actuator on the top side

the second moment of area, I. In this case, the bending stiffness of the nanometal coating will likely be around two orders of magnitude larger than that of the polymer substrate, because of the large difference in modulus.

Due to the configuration of the actuators in the design as well as the overall size scale of the propeller, only two types of actuators would realistically be viable for this design. The first would be a piezoelectric actuator, specifically in the form of a stripe actuator. This is because stripe actuators are designed such that one ceramic layer expands while another contracts which causes the actuator to flex [17], lending it to a bending application better than a stack actuator. The second type would be an SMA, such as nitinol, in the form of a strip. In this particular design, either a one-way or a two-way SMA would be workable. The shape only needs to change from its deformed configuration to its fully extended configuration, meaning only one shape needs to be remembered by the SMA.

In the initial concept, the actuators would be placed on the surface of the propeller blade. This would be detrimental to the aerodynamic performance of the propeller since the extra layer of the actuator on top of the optimized design would be an additional source of drag, making the propeller less effective. In addition, the actuators require some electrical connection in order to induce actuation. If these connectors are external to the structure as well, performance would be reduced even further. Thus, to avoid this, the actuators and the electrical connections need to be embedded within the structure itself, either in the polymer layer or underneath it completely, internal to the structure. The embedding would be done prior to applying the nanometal layer to the polymer substrate. In the case of embedding the actuator within the polymer substrate, an extra layer of the polymer would need to be placed above the actuators and be sealed from any potential fluid contact. This is due to the nature of the electrodeposition process where the entire structure is be placed in a bath where it may end up damaging the electrical connections or the actuators themselves. It would also ensure that the nanometal layer would be deposited only where it is desired. The electrical connections would run along the span of

the propeller blade, completely internal to it. These connections would need to be attached to the inner structure such that they will not move. This would prevent any potential inertial changes due to these connections during the operation of the propeller, preventing additional performance losses. This could be done with a standard adhesive that bonds well with the polymer substrate while not impeding electrical conductance.

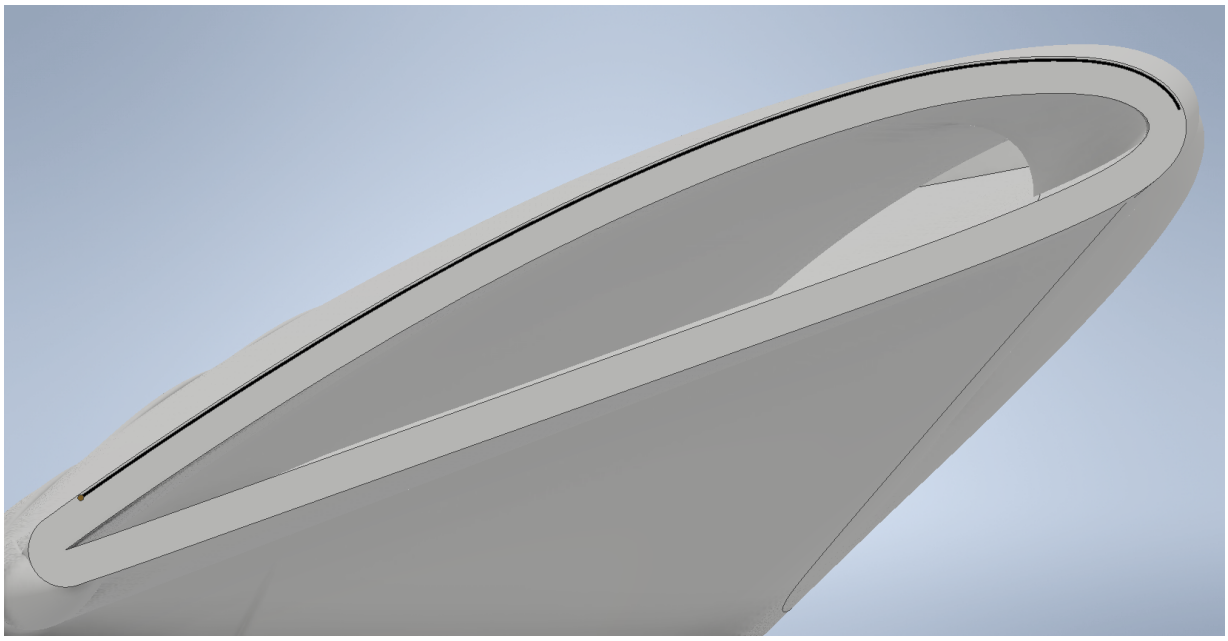

Figure 4.5: Section view of hollowed propeller blade showing an embedded actuator and slot for electrical connections

Figure 4.5 shows a section view of the updated design concept. It now features a hollow interior, with the actuators embedded within the structure itself. There is a thin section of the polymer directly between the top surface of the actuator and the free surface of the propeller blade, as discussed earlier. A slot to thread electrical connections through it was included at the end of the actuator near the trailing edge of the airfoil section profile. While the inclusion of an embedded actuator would increase the bending stiffness due to a higher stiffness of the actuator compared to the polymer substrate, it would still be less than placing it external to the structure. This is because the material would be closer to the bending axis, as well as having to remove some of the material of the substrate.

A degree of compliance can be introduced locally in order to assist with the change in twist angle. When the nanometal coating is being electrodeposited onto the propeller surface, it is possible to mask certain sections so that no material is electrodeposited. This will build up a layer of the nanometal where there is no masking. The masking can then be removed to allow those sections to be electrodeposited in addition to the sections that already have a coating of the nanometal. This would change local bending stiffness wherever this technique is employed, tailoring the structure to potentially better achieve the desired shape changes.

Despite all the efforts to reduce the bending stiffness of this structure, it would still remain fairly stiff. For a single section, isolated on its own, it may be fairly reasonable to actuate it. However, this is not a planar structure that has uniform forces being applied to it. In between the actuated sections,

the propeller blade remains a fairly rigid structure. These non-actuated sections will negatively impact any attempts to change the twist angles, even with tailoring the nanometal coating thickness. This isn't to say that achieving the desired shape changes is impossible, only that it may not be practical. The purpose of employing morphing into the structure is to improve the efficiency. That however, is at the cost of the actuation. If the net change in the flight time of a quadrotor is negatively impacted through the implementation of the morphing, then it is not feasible to do so.

Overall, this design is fairly simplistic, and relatively straightforward to implement. The polymer substrate could be 3D printed with vacancies in order to allow the actuators to be embedded. Connecting the electrical components to the actuators may be tedious given the small scale of the propeller. Care would need to be given to any potential soldering of these connections. When looking at VisiJet Crystal, the melting point of this polymer is stated to be between 55°C and 65°C [30], and soldering is typically done at a temperature much higher. While the polymer does not provide structural strength, melting part of the actuator seating may create enough space such that the actuator has room to extend before coming into contact with the surface above it. This could lead to a reduction in the actuation force available, and thus the change in the twist angle not reaching its desired target.

The next step to implement this design would be sealing the actuator off with a layer of the polymer substrate. This would have to be done with adhesive. This adhesive would need to be selected carefully according to two different criteria. First, it would need to bond well with both the polymer as well as the nanometal coating. For the polymer, it would ensure that the layer being glued cannot move. For the coating, it would ensure that the nanometal could be electrodeposited onto it, as well as there being no problems with delamination of the coating. If the coating cannot be electrodeposited onto the adhesive, there will be discontinuities. This would be detrimental as almost all of the strength of the structure is provided by the coating. Also, this would significantly change the local bending stiffness and result in unexpected shape changes due to actuation. Second, the peel strength of the adhesive would need to be high enough such that the actuation of the structure would not result in debonding.

The root of the propeller blade is intended to be attached to the hub of the propeller itself. As such, it shouldn't be coated in order to allow for this connection. This would be prevented by masking this end section. For this solid body design, it cannot have a relatively thick nanometal coating due to the continuous nature of the design, and the stiffness that would be associated with it. However, if the coating is too thin, it may not properly withstand the forces it would experience. This poses the design with a limited design space for the coating, even potentially making this design not viable altogether.

4.2 Design 2 - Rigid Wireframe Body

The idea for this design begins with a wireframe structure comprised of a polymer substrate and coated with a nanometal. The actuators in this design will be embedded within the structure like the previous design. Images illustrating this concept can be seen in Figures 4.6, 4.7 and 4.8.

The main idea in this design is to use as little material as possible in order to reduce the structure's bending stiffness as much as possible. The main way this is done is by keeping the connections between the discrete sections to a minimum. Instead of having a continuous connection along the entire airfoil profile, there are two wire-like connections running across the span of the propeller blade; one at the leading edge and one at the trailing edge. If the actuators are embedded as in the first design, then this design will actuate in the same manner. However, the rigid wireframe design allows for variation

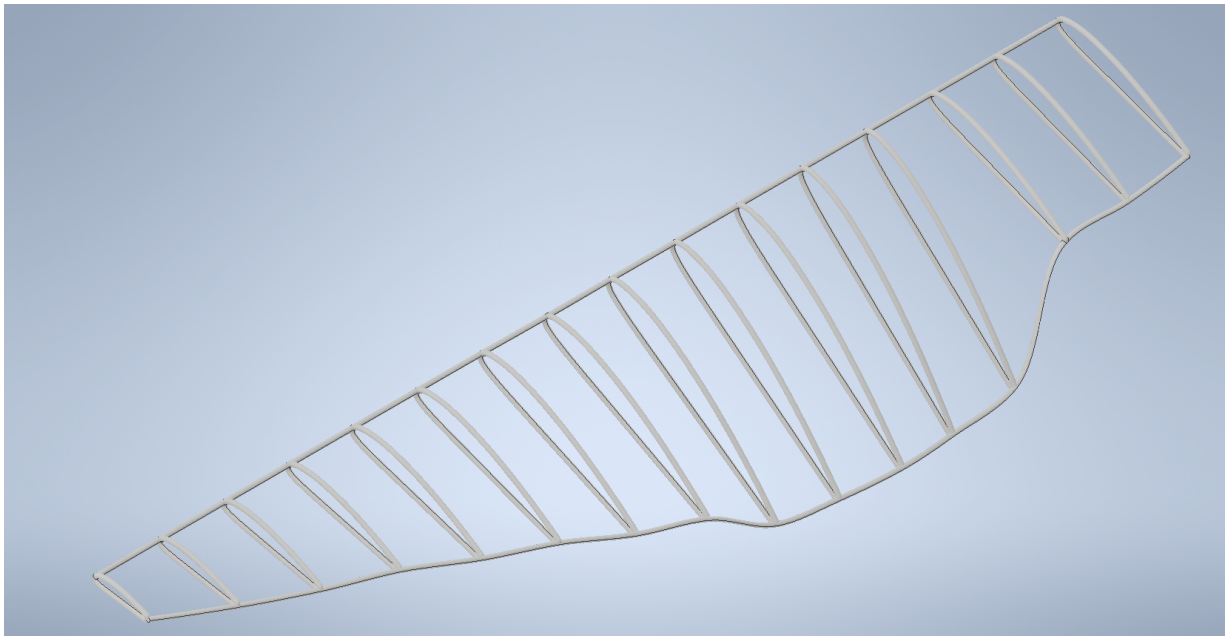

Figure 4.6: Isometric view showing top side of the wireframe propeller blade

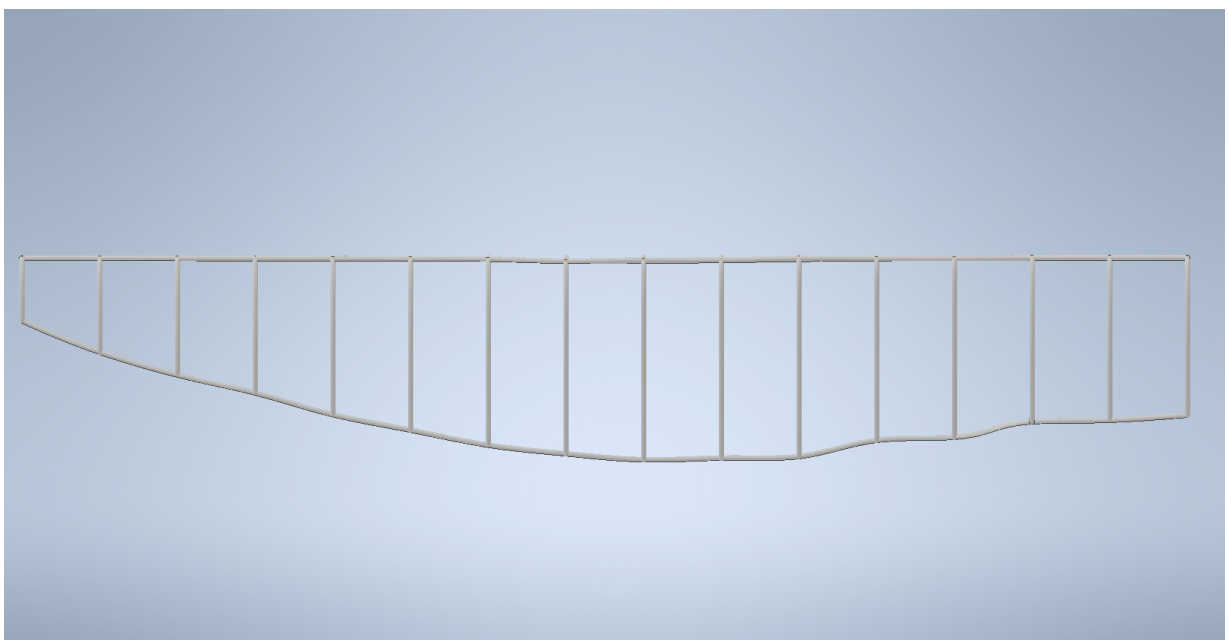

Figure 4.7: Top view of the wireframe propeller blade

in terms of how it is actuated. Linear actuators can be embedded within the structure, exerting a force along the length of the wireframe section itself. Since each wireframe section is connected by its leading edge and trailing edge, the force exerted by the actuator will cause the wireframe section to alter its shape, changing its twist angle. For this case, it would be beneficial for the section of the wireframe section where the actuator is embedded to be removed entirely. An image illustrating this can be seen in

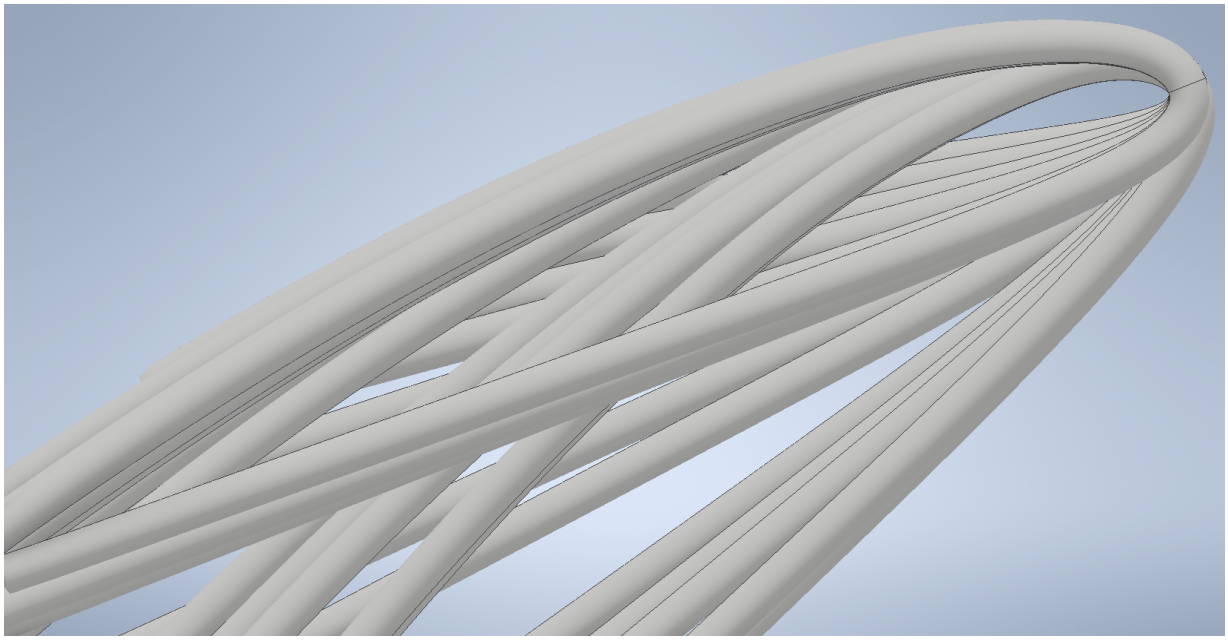

Figure 4.8: Side view showing highlighting the wireframe sections

Figure 4.9. The removal of the section would prevent the actuator from having to deform any material immediately encompassing it and dedicate its actuation force solely to changing the wireframe section's shape, and thus the twist angle.

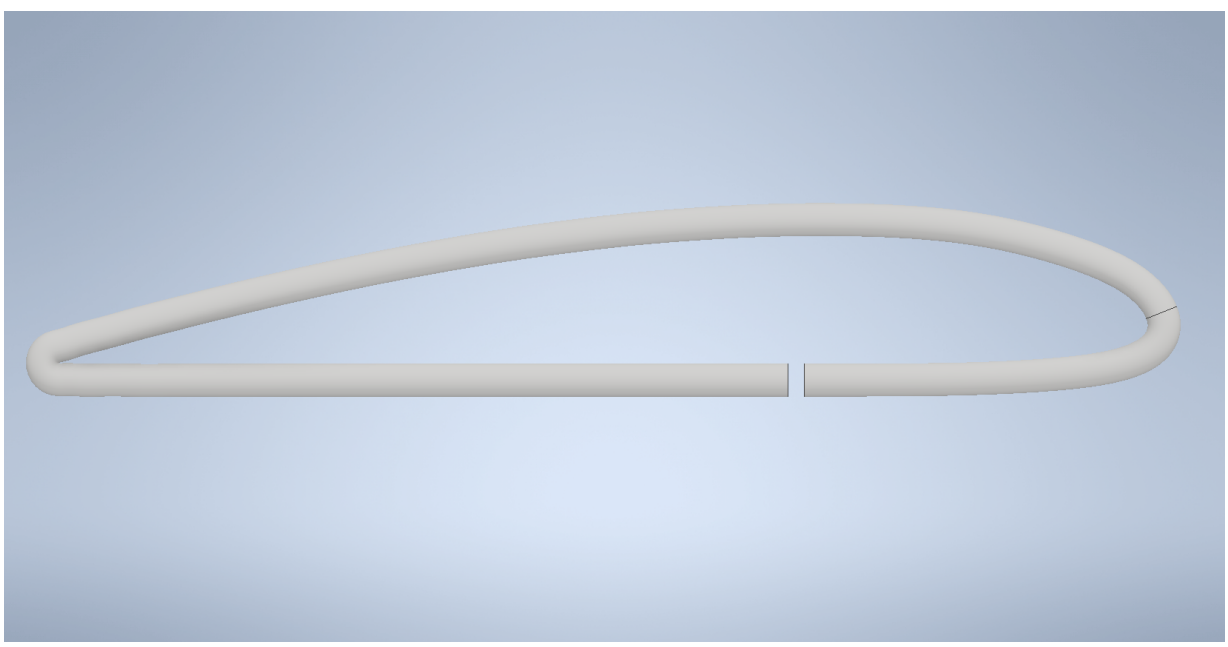

Figure 4.9: Side view showing a single wireframe section with a section removed for actuator placement

The main benefit of moving from a stripe actuator or an SMA actuator in the form of a strip to

linear actuators is that the actuation force capabilities are much larger. This is due to the fact that the force exerted would be along the axis of the actuator rather than perpendicular to it. This would mean that either a larger deflection can be achieved, or less voltage is required by the actuator to achieve the same deflection. With respect to larger deflections, this increases the likelihood of the design being able to achieve the desired shape changes. In the case of the lower voltages being required, this increases the viability of morphing providing a net positive in terms of performance for a quadrotor.

As in the solid body design, having the electrical connections move around could result in inertial losses of the propeller. The rigid wireframe design would presents the opportunity for the electrical connections to be routed completely internal to the frame itself. Figure 4.10 shows a section view of a single wireframe section from the side, highlighting where the electrical connections would run. This would also be the case for the wire-like connections that join the wireframe sections together at their leading edges and the trailing edges. Again, like in the solid body design, hollowing out the core of the rigid wireframe design would marginally decrease its bending stiffness while reducing mass overall.

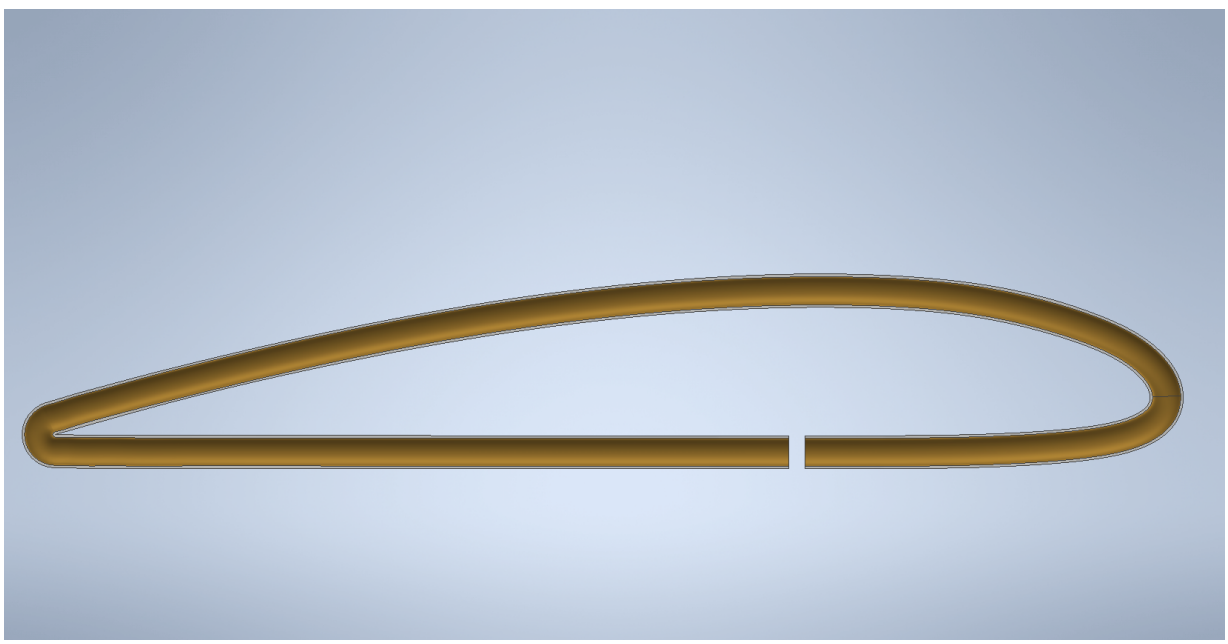

Figure 4.10: Side section view showing a hollowed out single wireframe section, highlighting potential electrical connection placement

The main drawback of this design is the fact that upon actuation, the entire wireframe section would be changing its shape. This would mean that the airfoil profile used to design the propeller blade would not retain its shape, affecting not only the twist, but also the chord and camber. This could have a negative effect on the aerodynamics of the propeller, making it operate below the optimized level that was previously determined. Another drawback of this design is that an axial force is being used by the actuators to induce a deflection that is out of plane. This is a fairly inefficient use of the force provided by the actuators. Next, using this kind of linear actuation to push outwards on the wireframe section can only increase the twist angle of a wireframe section. As a result, if the twist angle needs to be decreased, the initial shape of this rigid wireframe design would need to be changed. This would involve having the initial twist angle of each wireframe section in its lower magnitude configuration, regardless

of whether the flight condition were to be hover or forward flight. The sections that are in their incorrect configuration would then need to be actuated to return the propeller blade to its correct twist profile for the relevant flight regime. In addition, this would complicate the electrical system, where it would need to individually actuate certain sections rather than either actuating the entire structure or not. Lastly, this design would necessitate the use of a morphing skin in order to be capable of generate sufficient lift.

This rigid wireframe design is more difficult to implement than the solid body design would. There could potentially be a minimum size limitation on the 3D printing of the model depending on the sizing of features in this design, such as the thickness of the walls of the airfoil profile section. Either sizes would need to be increased, increasing mass or a higher fidelity printer would need to be used, most likely increasing the cost of the part. It was previously stated that the electrical components would be run through the hollow interior of the wireframe sections. In practice, this would not be a simple task to achieve. There are not any continuous paths without bends for the electrical connections to follow, so they would likely get snagged. One potential way to make the process easier would be to split the structure into a top half and a bottom half and print each section separately. The electrical connections could then be inserted with relative ease and connected to the actuators. The two structural sections would then need to be bonded together. Again, the adhesive would need to have good bonding properties with both the polymer substrate as well as the nanometal coating. Also, end caps would need to be placed at the cutout sections in order to give the actuator a larger surface to apply its actuation force against. This would need to be placed after the wires are housed within the structure.

Comparing this design to the solid body one, it is much less stiff overall, in addition to having less mass. While the reduced stiffness helps in terms of morphing, this can potentially result in unexpected shape changes. When the actuators are engaged, they push against the airfoils to expand them, and the resulting deflections of these profiles will also cause a deflection of the wire-like connections at the leading edge and trailing edge. These deflections are not expected to be very large, but any change can detrimentally affect the aerodynamics of the propeller by altering the flow of air around the airfoil sections. This problem can be alleviated by increasing the stiffness of certain areas. In the solid body design, compliance was added in morphing critical sections by first masking these sections, then allowing for the electrodeposition. In the rigid wireframe design, once the desired coating thickness is reached in the airfoil sections, they may be masked while further electrodeposition is performed on the remaining structure.

4.3 Design 3 - Rotating Wireframe Body

The idea for this design begins similar to the rigid wireframe design with the discrete airfoil profile sections being a wireframe. The connections between the sections however, are not at the leading edges and trailing edges, but rather at the centers of each section's chord line. This connecting rod would go through a connecting bar that would run from the leading edge to the trailing edge of each individual wireframe section. The central connecting rod would be used to facilitate the rotation of each individual wireframe section, but would not be rigidly connected to the sections themselves. Actuators would be used to enable the rotation of the airfoil profile sections around the central connection rod. Images illustrating this concept are shown in Figures 4.11, 4.12, and 4.13.

The way morphing occurs in this design starts by adding small caps to the sides of the each wireframe section. These are multipurpose, in that they will prevent lateral movement of the wireframe sections,

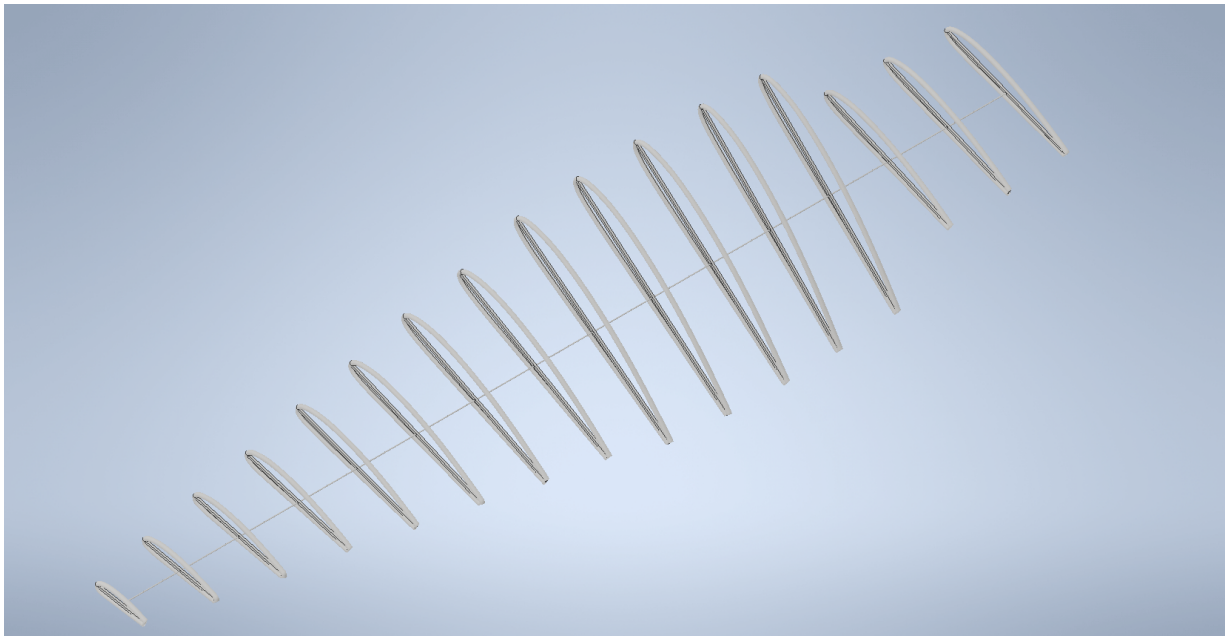

Figure 4.11: Isometric view of the rotating wireframe design

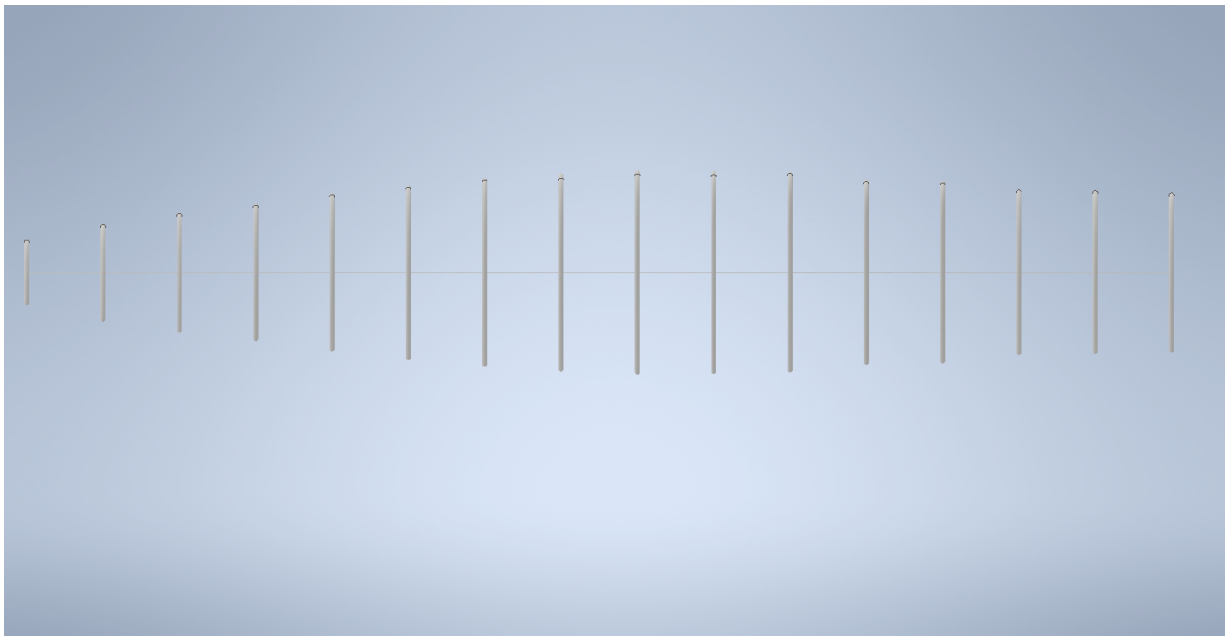

Figure 4.12: Top view of the rotating wireframe design

while acting as a guide for the morphing and limiting the twist angle change. The caps would feature a small cutout, providing the housing for the actuators as well as providing a physical limit to the actuation, which would be the initial and final twist angle for the wireframe section. On both sides of the connecting bar, there would be a protrusion which would be the site for the actuation, and ultimately allowing for the controlled rotation around the central connecting rod. A closer look at the mechanism

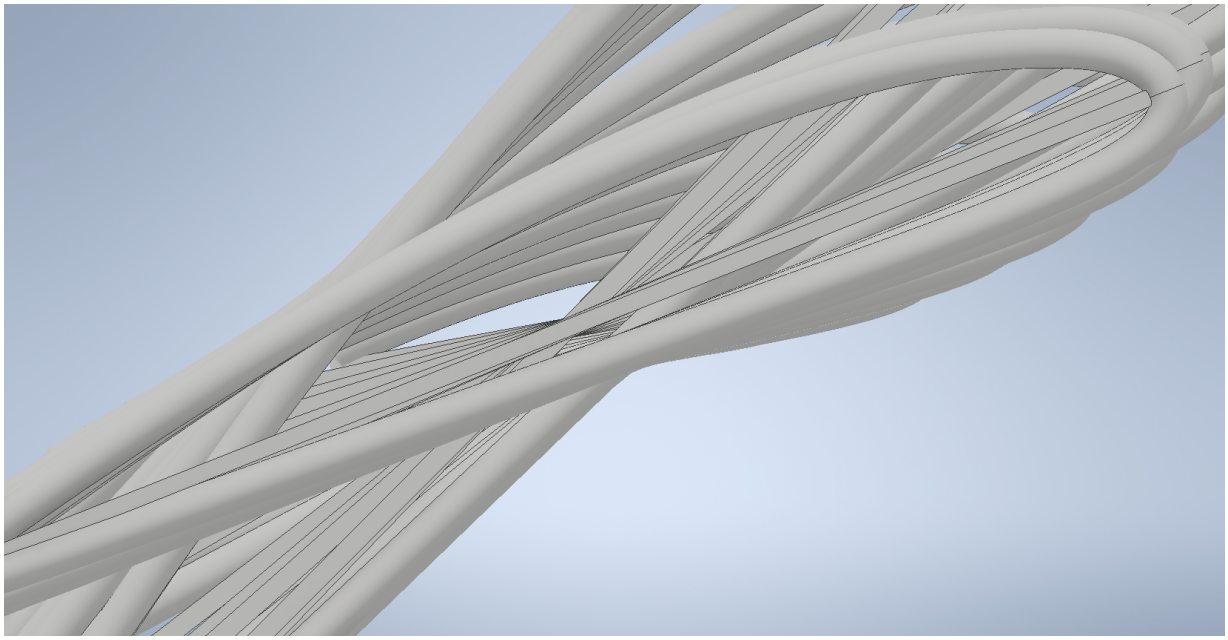

Figure 4.13: Side view of the rotating wireframe design

enabling the morphing is shown in Figures 4.14 and 4.15, with an assembled version shown in Figure 4.16. A fillet was added to the protrusion in order to limit stress concentrations that would arise from the actuation. As a result, the same material that was added to the protrusion needed to be removed from the cap so that it would not decrease the actuation range.

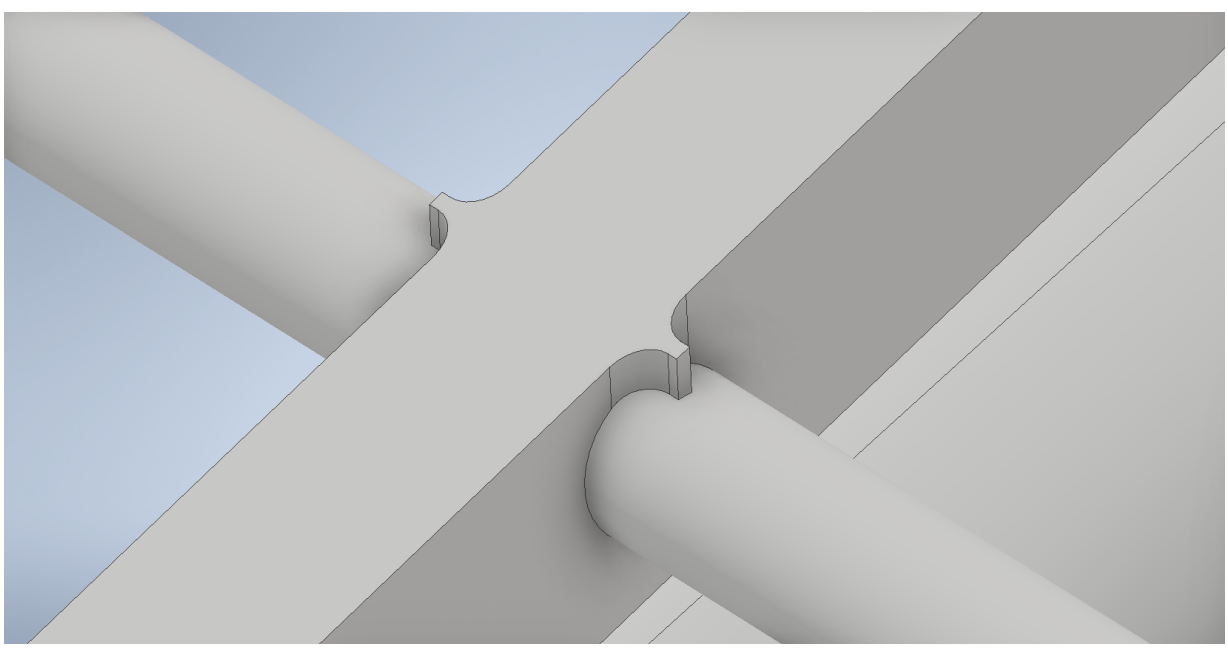

Figure 4.14: Isometric view of a wireframe section showing protrusions on the connecting bar

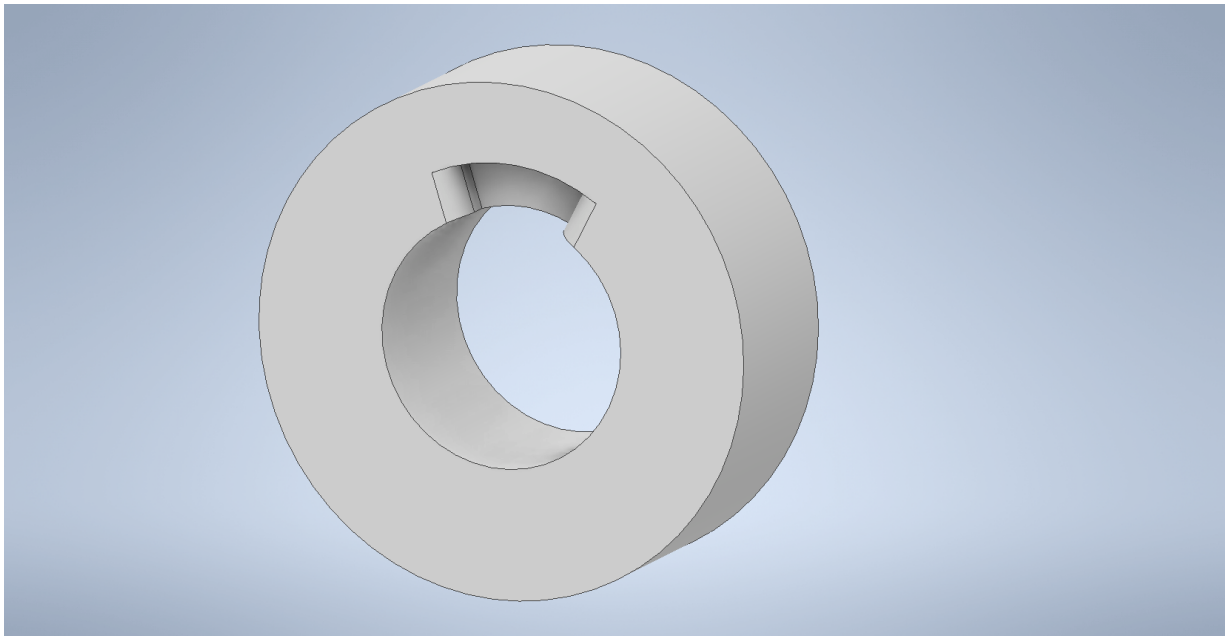

Figure 4.15: Isometric view of the cap showing the cutout for the actuator

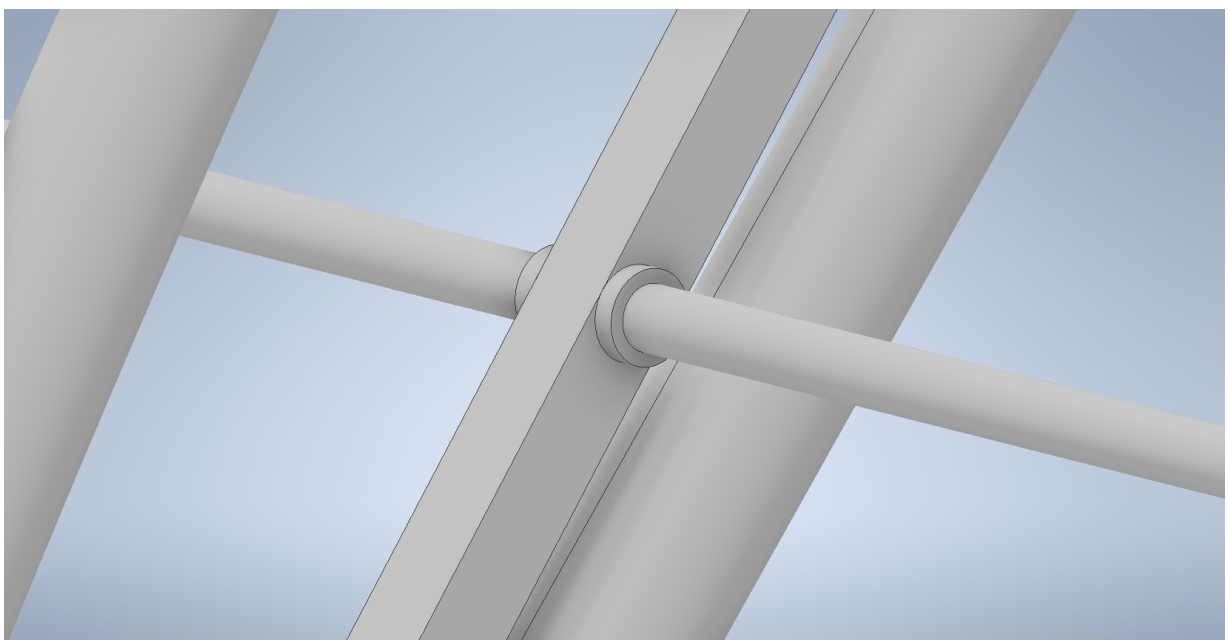

Figure 4.16: Isometric view of a wireframe section showing the assembly with the caps

This rotating design shares the benefits of the rigid wireframe design, where it is fairly compliant through minimizing connections between the sections by using minimal materials. The wireframe sections in this design will be comprised of a polymer substrate with a nanometal coating. Again, this reduces the mass of the structure making it more efficient. In terms of actuation, linear actuators would perform best for this design, since most of the actuation and resulting morphing will occur in plane. For larger

twist angle changes, this is not the case and there will be some efficiency loss, however, linear actuators would still perform better than stripe actuators. Since no parts are rigidly connected, this design can be separated into individual parts. This can potentially make 3D printing of the design easier to accomplish. The way the 3D printer available works, an initial wax supporting structure is printed as a support for the intended structures being printed. After printing, this wax is melted away by placing the part in an small oven. However, some parts may have difficulty removing all of the wax, especially for fully enclosed structures that are hollow. This would add parasitic mass to the structure. Printing parts individually would make it easier to prevent this from happening. In addition to this, electrodepositing the nanometal coating onto the parts would be more reliable. Since smaller parts at a time could be coated, it would be much easier to achieve a uniform coating thickness on each part, as opposed to electrodepositing an entire structure at once.

A significant downside to this rotating design is the fact that the actuators will be absorbing a significant portion of the aerodynamic forces. This is because of the lack of rigid connections of the wireframe sections to the central connecting rod. As a result, actuation forces required for this design may be much larger. While this is occurring, the actuators are being required to achieve relatively high displacements. This would significantly limit the viability of actuators that could be implemented. A potential complication arises due to the central connecting rod. In this design, there is a significant amount of function associated with the rod. It allows for the caps to be slotted and is hollowed to enable the electrical connection to be embedded, all while being the backbone for the wireframe sections. With the rigid wireframe body design, there were two connections to add strength against bending stresses arising from lifting forces. With this, it would all be experienced by this single structural element with reduced sections. As a result, it may require a thicker nanometal coating to be applied to it. This adds mass and cost to the overall design. Finally, this model would again necessitate the use of a morphing skin.

In terms of implementation, this design can be tedious and complicated. All of the parts would need to be individually assembled, and the caps bonded to the central connecting rod. Again, the choice of adhesive is very important. Getting the positioning correct with respect to the twist angles would be difficult just by hand. To alleviate this, the rods and the caps can be made to be slotted, ensuring proper placement. For the sections, Images illustrating this can be seen in Figures 4.17 and 4.18. Housing the electrical components in this rotating design is easier than in the rigid wireframe design though. The central connecting rod can be made to be hollow with the electrical connections running through it. At the sections with the caps, a portion of the central connecting rod can be removed to allow for a connection to the actuators. In order for the actuators to stay in place, they would require some sort of groove, housing, or guide. This would also help with directing the actuation to be consistent.

Once the structure has been completely assembled, it would need to be electroplated. This is a slightly more difficult task than the previous designs. This is mainly due to the non-rigid connection of the wireframe sections to the central connecting rod and the caps. There cannot be a continuous connection of the nanometal coating between these parts or else morphing would be much more difficult to achieve. Instead of the actuators simply rotating the wireframe sections, they would additionally need to deform the nanometal coating. This could be alleviated by masking the section between these parts, however this would create a small gap for which the wireframe sections could move laterally on the central connecting rod. It would also be a site for which failure would be more likely to occur since it would be uncoated and have less strength. Thus, it would be more prudent to electrodeposit

each individual wireframe section with the protrusions being masked, as well as the surfaces of the caps that would not be in contact with central connecting rod or the protrusions. These parts could then be assembled onto the non-electroplated central connecting rod. The rod would still need a nanometal coating in order to provide strength. In order to prevent the already coated wireframe sections and caps from increasing their coating thicknesses, they would need to be masked.

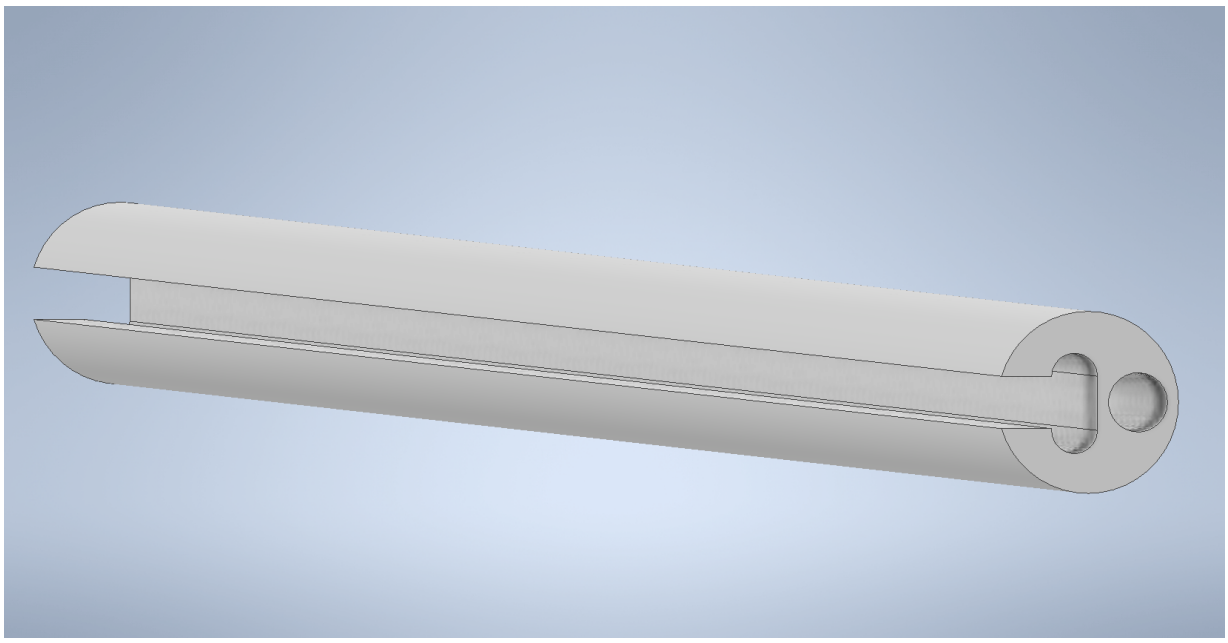

Figure 4.17: Isometric view of the hollowed central connecting rod with a slotted section added

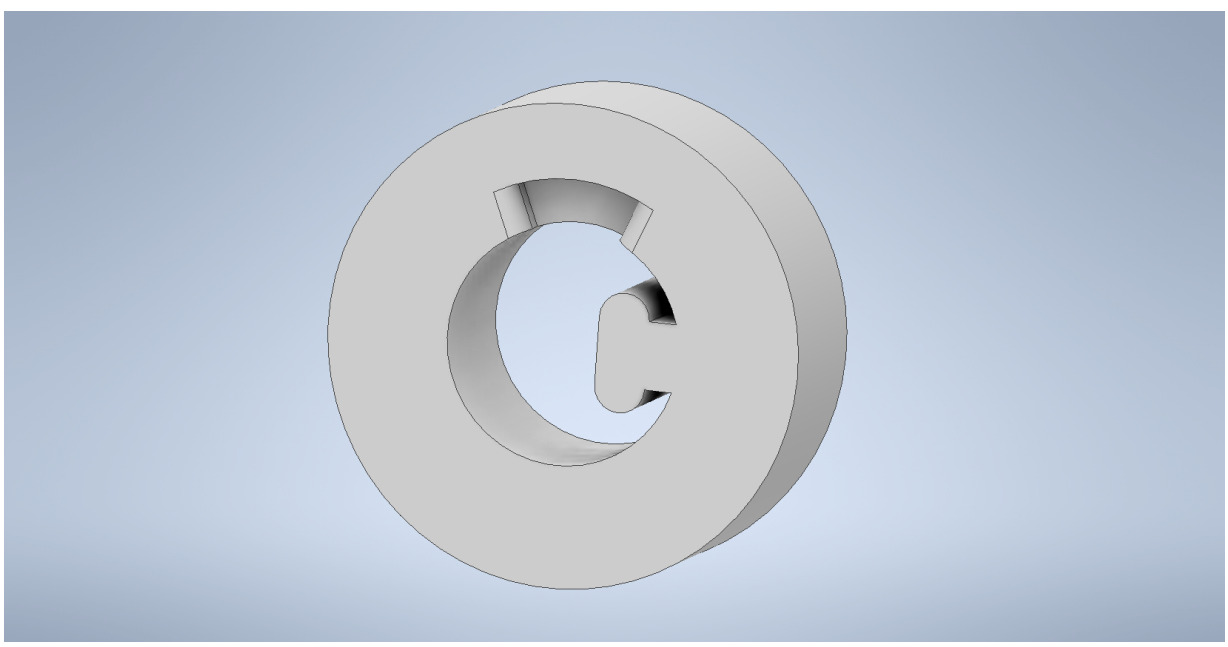

Figure 4.18: Isometric view of a the cap with a slot cut out

4.4 Design Discussion

During the design process, different tradeoffs are constantly being made. This can be seen by comparing all of the designs for what benefits they provide versus what is given up to achieve that. In the solid design, simplicity of the design is traded for a higher structural stiffness and mass. It is the opposite for the rigid wireframe design, where structural compliance is traded for complexity of the structure. In the rotating wireframe design, staying as true to the generated shapes as possible is traded for high performance demand of the underlying actuators. All of these tradeoffs arise from the fact that morphing capabilities in the propller is desired. This decision was made in order to improve the performance and efficiency of a quadrotor. This in itself is another tradeoff, where structural function is desired, which will result in a higher cost compared to a non-morphing propeller. This is not to say that making tradeoffs are bad, but rather to understand that tradeoffs are inevitable. They need to be taken into account during the design process and decisions need to be made in order to determine the most suitable design for a given application.

Some important concepts that needs to be discussed are fatigue and creep. The structure undergoing morphing to change its shape and back is a cyclic stress. During the operation of a quadrotor, this can potentially occur quite frequently. This could significantly affect the operating lifespan of the propeller blade, either through the polymer substrate, the nanometal coating, or even the chosen actuator. Currently, fatigue characteristics of VisiJet Crystal and the nanocrystalline nickel coating are unknown so no analysis can be performed. As for creep, if an SMA is chosen as the actuator, it can be potentially be exposed directly to the polymer substrate. In order to induce actuation in an SMA, resistance heating is used. If the temperature is high enough in the SMA, even locally, it can begin to cause creep in the polymer substrate. This could affect the actuation of the SMA and potentially cause the actuator to be less effective in achieving the desired morphing. These concepts are important to take into account for the implementation of a chosen design.

The next step will be taking one of the designs that was developed and undergoing a finite element analysis. This will aid in evaluating the viability of that design while simultaneously understanding the magnitude of the actuation being required in order to achieve the desired morphing. It will also provide feedback for the design if it will in fact behave as was theorized in this chapter. All of this information can then be applied back to the model and adjust it if necessary.

Chapter 5

Finite Element Model

The rigid wireframe body from Chapter 4 was selected for the finite element analysis. This design requires the actuation force of the actuators in order to induce morphing. As a result, the structure will undergo a deformation in order to achieve its desired shape change. In addition, the wireframe body design seems very likely to successfully morph with a reasonable actuation force. The other designs fall short in at least one of these areas. All of these factors create a compelling case for the wireframe body design to be selected as the subject of the detailed analysis.

To understand the actuation force required to reasonably morph the structure, a separate analysis will be performed on a double wireframe profile section. While it is understood that the physics won't be the same for a double section versus the entire model, it will aid in providing the general magnitude required as well as the behaviour exhibited. In addition, it will provide the opportunity to perform a mesh convergence analysis on a smaller part to get an understanding for the mesh density required to achieve an accurate result before performing the finite element analysis on the full model. For the analysis, the model will only consist of the nanometal coating and not the polymer substrate. The main reason for this is that the substrate provides virtually no strength to the structure. Adding it in provides almost no benefit, while complicating the model much more than necessary.

5.1 Model Details

The first step for the analysis is to have a model with all of the required features. This model was created using Autodesk Inventor 2020. To generate the airfoil profile sections, the Cartesian coordinates base NACA 2412 airfoil were determined. 68 points were used, starting from the trailing edge moving counterclockwise around the profile. The values are shown in Table 5.1 and plotted in Figure 5.1.The geometric coordinates of the profile are normalized between 0 and 1 on the x-axis, so each discrete section needed the NACA 2412 profile coordinates to be multiplied by its associated chord value to size it correctly. Next, a rotation matrix

$$R = \begin{bmatrix} \cos\theta & -\sin\theta \\ \sin\theta & \cos\theta \end{bmatrix} \tag{5.1}$$

was used to transform the chord-adjusted coordinates, where the input for θ is the compliment to the twist angles generated in Chapter 3, since the rotation matrix crates a counterclockwise transformation.

The values for the first discrete section are shown in Table 5.2 and plotted in Figure 5.2.

x	y
1	0
0.99572	-0.00025
0.98296	-0.00094
0.96194	-0.0019
0.93301	-0.00302
0.89668	-0.00429
0.85355	-0.00575
0.80438	-0.00741
0.75	-0.00928
0.69134	-0.01131
0.62941	-0.01345
0.56526	-0.01566
0.5	-0.01792
0.43474	-0.02018
0.37059	-0.02242
0.33928	-0.02351
0.30866	-0.02458
0.27886	-0.02559
0.25	-0.02653
0.22221	-0.02734
0.19562	-0.02795
0.17033	-0.02832
0.14645	-0.02839
0.12408	-0.02816
0.10332	-0.02763
0.08427	-0.0268
0.06699	-0.02567
0.05156	-0.02414
0.03806	-0.02214
0.02653	-0.01959
0.01704	-0.01651
0.00961	-0.01296
0.00428	-0.00898
0.00107	-0.00453

x	y
0	0.00047
0.00107	0.00616
0.00428	0.01254
0.00961	0.01943
0.01704	0.02652
0.02653	0.03352
0.03806	0.04027
0.05156	0.04677
0.06699	0.05313
0.08427	0.05939
0.10332	0.06552
0.12408	0.07134
0.14645	0.0766
0.17033	0.08113
0.19562	0.08483
0.22221	0.08774
0.25	0.08996
0.27886	0.09158
0.30866	0.09266
0.33928	0.09318
0.37059	0.09312
0.43474	0.09128
0.5	0.08719
0.56526	0.08105
0.62941	0.07319
0.69134	0.06405
0.75	0.05412
0.80438	0.04394
0.85355	0.034
0.89668	0.02475
0.93301	0.01656
0.96194	0.00972
0.98296	0.00448
0.99572	0.00115

Table 5.1: Cartesian coordiantes for NACA 2412 profile

This process was repeated for every discrete profile section and its resultant twist angle for the twist angle that is the lower value between the hover and forward flight conditions. Recalling Chapter 4, the morphing in this design can only increase the twist angle. So the generated profile contains some sections that are the optimal ones for the hover condition, and some for the forward flight condition. This means that in the finite element simultaion, only certain sections will undergo actuation at a time.

Once this process was complete, the discrete profile sections were imported into Autodesk Inventor according to their position along the span of the propeller blade. The 16 sections were spaced 6.858 mm apart, equating to a 114.3 mm radius for the propeller, taking into account the 2.54 mm offset due to the propeller hub that was assumed. A spline curve was used to create a smooth airfoil profile, interpolating between the imported points for each section individually. Next, a wireframe was created on each section to form the structural airfoil profile by sweeping a circular section tangent to the spline curve previously

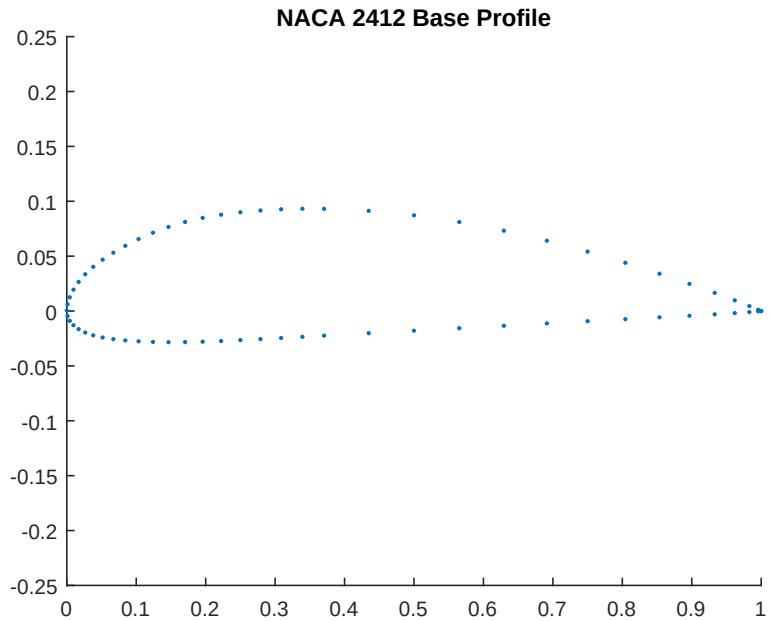

Figure 5.1: NACA 2412 plotted coordinates

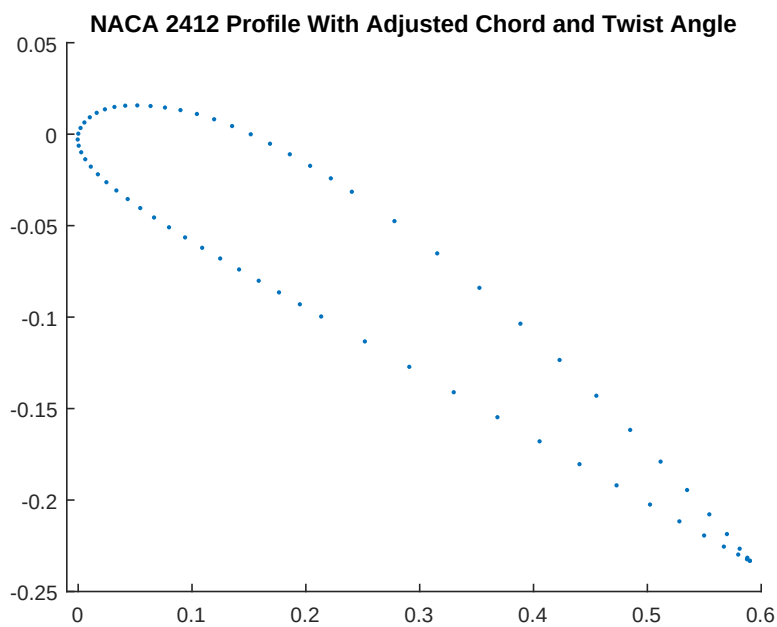

Figure 5.2: First discrete section plotted coordinates after transformation

x	y
0.590085729	-0.233214671
0.587501858	-0.232364033
0.579811446	-0.229795373
0.567183958	-0.225459683
0.549851578	-0.219373679
0.52811758	-0.211650399
0.502326689	-0.202453375
0.472925038	-0.191965752
0.440400064	-0.180386999
0.40531221	-0.1679045
0.368269121	-0.154724299
0.329899717	-0.141067667
0.290863657	-0.127181672
0.251827598	-0.113295676
0.213451197	-0.099656747
0.194721409	-0.092997989
0.176403444	-0.086488348
0.158583343	-0.080134537
0.141334247	-0.073958642
0.124746861	-0.067955576
0.10891422	-0.06211435
0.093904663	-0.056434683
0.07979709	-0.050906822
0.066650512	-0.04555409
0.054523936	-0.040399808
0.043476371	-0.035467298
0.033543222	-0.030770551
0.024795018	-0.026269218
0.01729529	-0.021940648
0.011086299	-0.017746965
0.006204687	-0.013716293
0.002648262	-0.009888704
0.000431299	-0.006297129
-0.000425071	-0.002922628

x	y
0.000109611	0.00027734
0.002067994	0.003385388
0.005450079	0.006401516
0.010202085	0.009224173
0.016239914	0.011675096
0.02347233	0.013592488
0.031850218	0.014886602
0.04133227	0.015573761
0.051920538	0.015728204
0.063577144	0.015392191
0.076247883	0.014566677
0.089855372	0.01315944
0.104282299	0.011046278
0.119430008	0.0081502
0.135216171	0.004435518
0.151585205	-4.85102E-05
0.168501424	-0.005219556
0.185909106	-0.010994192
0.203745532	-0.017306697
0.221935229	-0.024140885
0.24039682	-0.031478242
0.277821705	-0.047524721
0.315376852	-0.065157761
0.352453908	-0.084000477
0.38847484	-0.103599271
0.422887267	-0.12343564
0.455185875	-0.142975563
0.484900611	-0.16166485
0.511596973	-0.178997468
0.534890134	-0.194514309
0.554417921	-0.2078198
0.569893913	-0.218602887
0.58107547	-0.226597109
0.587828359	-0.231537913

Table 5.2: Cartesian coordiantes for the first discrete section after transformation

generated. A similar sweep with a smaller circular section was done in order to remove material making each section hollow. The left an inner radius for the wireframe of 4.572 mm with a wall thickness of 0.254 mm. This would allow for a maximum 25 gauge wire to be housed inside the wireframe sections.

For the wire-like connections for the leading and trailing edges, a circular section was created the tip of each leading edge and trailing edge, again with an inner radius of 0.4572 mm and a wall thickness of 0.254 mm. A loft was performed in order to form a smooth connection between each of the circular sections. This was done for both the leading edge and trailing edge. Last, a cutout was created in each discrete wireframe section to allow for an actuator to be placed. This cutout was placed at the halfway point of the chord length for each section, with a cutout length of 0.508 mm.

For the double wireframe section model, two sections created from the full model were kept with the other sections being removed. In addition, the wire-like connections were removed apart from the connection between the two sections. The cutout section for the actuator was kept in the model.

5.2 Double Wireframe Section Morphing Analysis

5.2.1 Analysis Setup

Two wireframe sections were imported into Abaqus, specifically the first and second wireframe section. The first section will remain rigid, while the twist angle of the second section will change from 31.17° during hover to 33.27° during forward flight. The properties of nanocrystalline nickel were applied to the model, with the Young's modulus, $E = 200$ GPa and Poisson's ratio, $\nu = 0.31$. For the mesh, quadratic tetrahedral elements were required to be used as there are features with rapid geometrical changes, curved surfaces, and the model is not a standard, simple shape. The model was then meshed, creating 261617 elements. This can be seen in Figure 5.3.

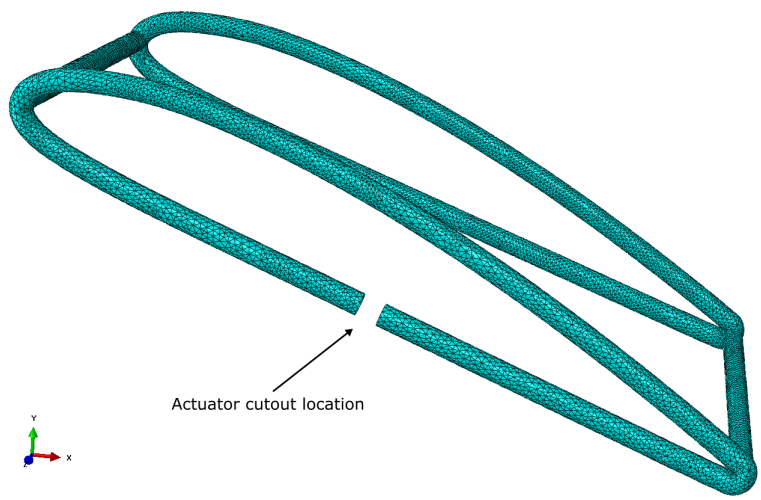

Figure 5.3: Meshed double wireframe section showing the location for the actuator

The nanocrystalline nickel coating thickness is thin on an already small part. In order to create a proper, functioning mesh, very small mesh sizes must be used. Thus, meshing the part with more elements becomes potentially computationally expensive. A greater number of elements means a greater number of equations the FEA software needs to solve. While increasing the number of elements will increase the accuracy of the analysis, increasing the number elements past a certain mesh density will yield decreasing returns on the improvement in accuracy. The tradeoff for improved accuracy is increased computation time. Determining a mesh density that provides an acceptable level of accuracy for the computation time will be the basis of the mesh convergence analysis.

The next step is to simulate the loads that would be applied by the actuators. These will be acting on the faces of the cutout section in the wireframe section as shown in Figure 5.4. The loads were applied to the surface as a pressure, assuming that the actuator will evenly distribute its force across this surface, and directly perpendicular to it. The magnitude of the pressure applied is 30 MPa. For the section it is being applied to, this approximately equates to a 10 N actuation force. The last step before running the analysis is to apply the boundary conditions. For the full model, the first section of the propeller blade would need to be connected to the hub of the propeller. This connection would need to be rigid such that no air could flow through a potential gap, causing an irregular flow. This would be detrimental for the propeller, and would reduce if not negate any gain made through an optimized,

morphing propeller. As such, the first section would not likely be able to morph. While this does mean that the potential performance gain is not the maximum that it could be, since the twist angle change is relatively small, there would still be a benefit to morphing. In terms of boundary conditions, the first wireframe section is set such that it does not displace. This allows the wire-like connections to displace, in addition to the second wireframe section. At this point, the simulation is ready to run.

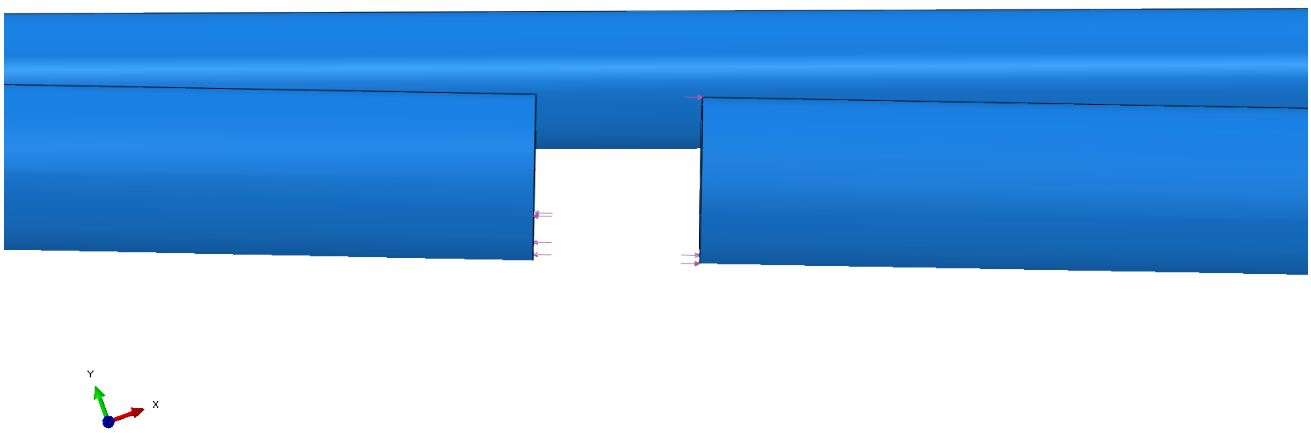

Figure 5.4: Load state for double wireframe section

5.2.2 Double Wireframe Section Morphing Results

The simulation results can be seen in Figure 5.5. The first notable result is that the magnitude of the stress in the entire structure is fairly uniform in distinct sections. For the first wireframe section, stresses are low due to there being no forces acting nearby, and no change in the shape. Stresses in the second wireframe section can be divided into the upper loop and the lower loop. In the upper loop, the structure is bending flattening, resulting in higher stresses and deflections. In the lower loop there is less deflection as well as lower stresses since less bending is occurring in this portion of the structure. This is likely due to the disconnect in this portion due to the actuator placement. The stresses in the trailing edge wire-like connection are fairly uniform. The magnitude is higher than the lower portion of the second wireframe section but lower than that of the upper portion of the same section. This would indicate that some bending is likely occurring in this section. The stresses in the leading edge wire-like connection are not quite uniform. The magnitude on the lower half of this section are higher than that of the upper half, indicating that this section would be bending upwards in relation to the wireframe section. The highest stress in the model occurs at the sharp geometric change in the second wireframe section. However, this may be due to the mesh not being refined enough. It could also be due to the fact the sharp geometric change is causing a large stress concentration. Performing the mesh convergence analysis will provide a greater understanding into this.

The next notable thing is that a shape change does in fact occur in the model, however not in the manner predicted. The top side of the second wireframe section has displaced downwards, as have the lower sections but by a lower magnitude. This shows that morphing is occurring in the model as desired, but instead of increasing the twist angle, it has in fact decreased. Upon inspecting nodal displacements, the magnitude of the change in the twist angle is 0.45°. This specific wireframe section would require a change in the twist angle of 2.1°, meaning a larger actuation force would be required to achieve the desired twist angle change. This twist angle change could also be influenced by the placement of the actuators in the wireframe section. This is not only with respect to the upper or lower portion of the section, but also where along the chord line of the section that it is placed. This could potentially affect the required actuation force to achieve the desired twist angle change, or even the maximum amount of the twist angle change possible.

It was desired to investigate the effect of the placement of the cutout on the change in twist angle since there are many different locations that it may be placed. As such, more models of the selected wireframe sections were created with varying cutout placements. These placements chosen were the quarter chord point on both the top and bottom loops, the three-quarter chord point on both the top and bottom loops, and the mid chord point on the top loop, in addition to the original mid chord point on the bottom loop that was already simulated. Each model was meshed using the same mesh density, and with the same loads and boundary conditions applied to it. The results for the change in the twist angles for each are shown in Table 5.3.

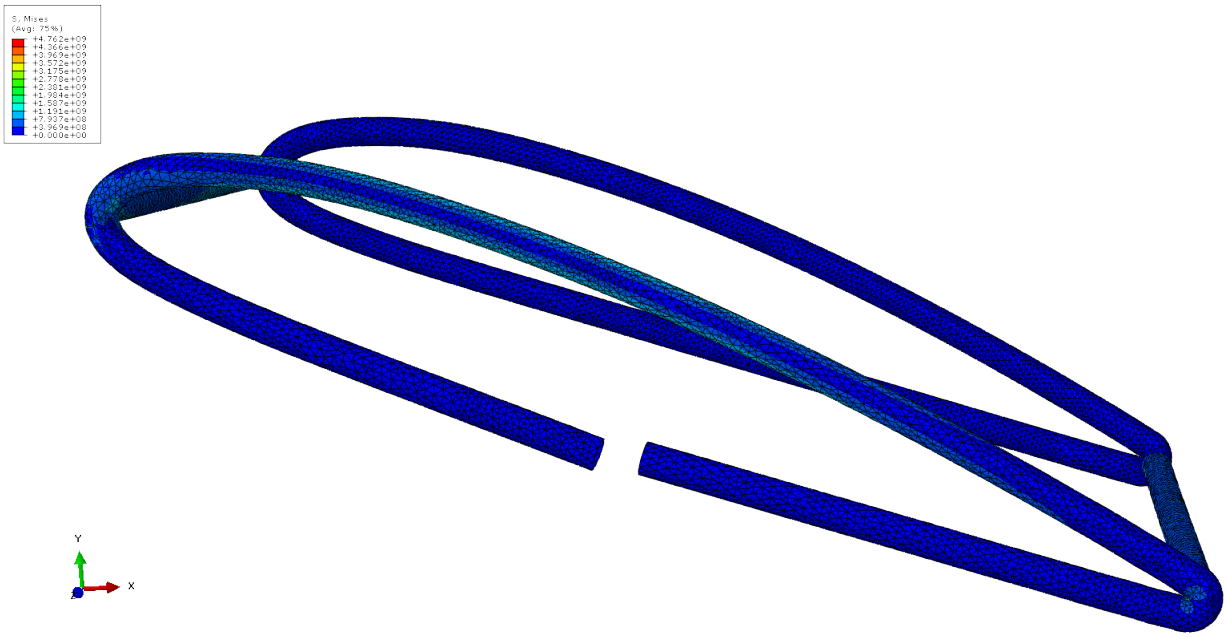

Figure 5.5: Stress state from morphing for the double wireframe section

From the results of all the simulations, the most effective placement for the actuator is the three-quarter chord point on the upper portion of the wireframe section. It achieves a twist angle change of 1.65°, getting much closer to the desired amount of 2.1° than all of the other cutout placements. It appears that a cutout on the upper portion of the wireframe section consistently results in an increase

Cutout Location Placement	Twist Angle Change (°)	Direction
Bottom, quarter chord	0.65	Decrease
Top, quarter chord	0.05	Increase
Bottom, half chord	0.46	Decrease
Top, half chord	0.91	Increase
Bottom, three-quarter chord	0.65	Decrease
Top, three-quarter chord	1.65	Increase

Table 5.3: Twist angle changes with varying cutout placements

of the twist angle, while a cutout on the lower portion results in a decrease. This would provide the opportunity to select the actuator cutout placement in a given wireframe section depending on whether the section needs to increase or decrease its twist angle. This would allow for the entire propeller blade to be in either its hover or forward flight configuration while having all of the actuators either engaged or not.

In all of the simulations, it is the part of the wireframe section that is closer to the leading edge that deflects the most. This is consistent with the stresses observed in the two wire-like connections. It seems that the capability for a wireframe section to change its twist angle is contingent on how effective the actuation force is in causing the upper portion of the section to bend. This is seen in the simulation results, where moving the cutout away from the half chord point on the bottom portion of the section increases the magnitude of the twist angle change. It is also seen through moving the cutout section towards the trailing edge in the upper portion, which leads to a much larger magnitude of change in the twist angle, and moving the cutout into the section that needs to bend leads to a very low magnitude of change in the twist angle. From these results, it would be more impactful to place the actuator cutout on the upper portion of a given wireframe section, closer to the trailing edge of the model rather than the leading edge.

5.2.3 Mesh Convergence Analysis

The next step was to perform the mesh convergence analysis in order to determine the minimum mesh density required to accurately predict the stresses and displacements in the model. For this, the model with the actuator placed at the three-quarter chord point on the upper portion of the wireframe section was used. The same material properties were used, with the Young's modulus $E = 200$ GPa and Poisson's ratio $\nu = 0.31$. Many meshes were generated, with the mesh density increasing with successive meshes. The total element count from the smallest mesh density to the largest spanned over an order of magnitude. A 30 MPa stress was applied to the actuation surfaces for each mesh. Boundary conditions were required in order to simulate the propeller being attached to the propeller hub. This was done by restricting the displacement and rotation of the half of the wireframe section without the cutout, furthest from the wireframe section with the cutout. These boundary conditions are illustrated in Figure 5.6

Once the loading state and the boundary condition were set, the simulation was run for each mesh. The results for each individual mesh can be seen in Table 5.4 and Figure 5.7. The absolute value of the percentage change in the Von Mises stress from one mesh to the next was determined for each simulation, using equation.

$$\%change = |\frac{(stress_2 - stress_1)}{stress_1}| \tag{5.2}$$

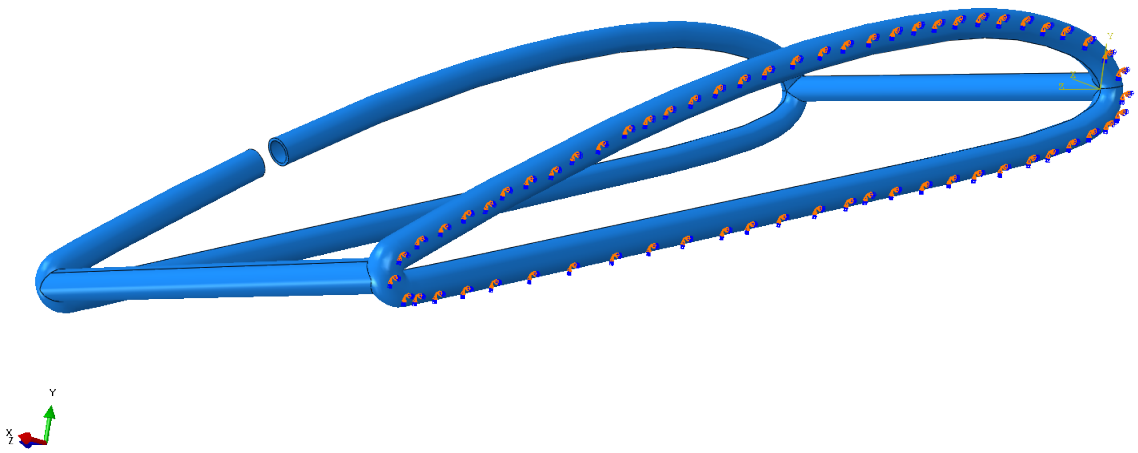

Figure 5.6: Boundary conditions applied to the double wireframe section

The results are shown in Table 5.5 and Figure 5.8. At a lower number of elements, the percent change in the stress for successive meshes are fairly large. As the mesh density increases, the variation in the stress reduces drastically. The stress seems to converge to approximately 86 MPa. The first mesh that approaches the converged value has 42736 elements, with a stress of 83.62 MPa. However, going to the next mesh density increases the accuracy of the resultant maximum stress. Going beyond this mesh density increases accuracy further, but with diminishing results. In addition, each increase in mesh density increases the computation time required to solve the finite element analysis. Considering the full model contains sixteen individual wireframe sections with two wire-like connections spanning its length, larger mesh densities could be very computationally expensive. As such, for the analysis of the full model, the mesh density of the double wireframe section with 63031 elements will be selected and implemented.

For each double wireframe section analysis, the maximum stress occurs at an element on the leading edge of the wireframe section with the cutout, on an internal surface where the wire-like connection meets the wireframe section. An example of this is shown for the model using 127543 elements in Figure 5.9. In this example, the maximum stress value is well below the yield stress for the nanocrystalline nickel coating, which can widely vary from 338 MPa to 917 MPa [9], while achieving a change in the twist angle close to that which is desired in the structure. However, larger desired changes in the twist angle will require a greater actuation force, resulting in greater stresses experienced within the structure. This will need to be monitored to ensure the viability of the design and its implementation.

Number of Elements	Maximum Stress Value (MPa)
10809	46.74
15156	82.93
17247	76.24
24733	69.16
29710	67.77
33373	69.31
42376	83.62
63031	85.15
77652	84.84
87714	86.46
98879	84.55
106866	85.76
127543	86.07

Table 5.4: Von Mises stress values for varying mesh densities

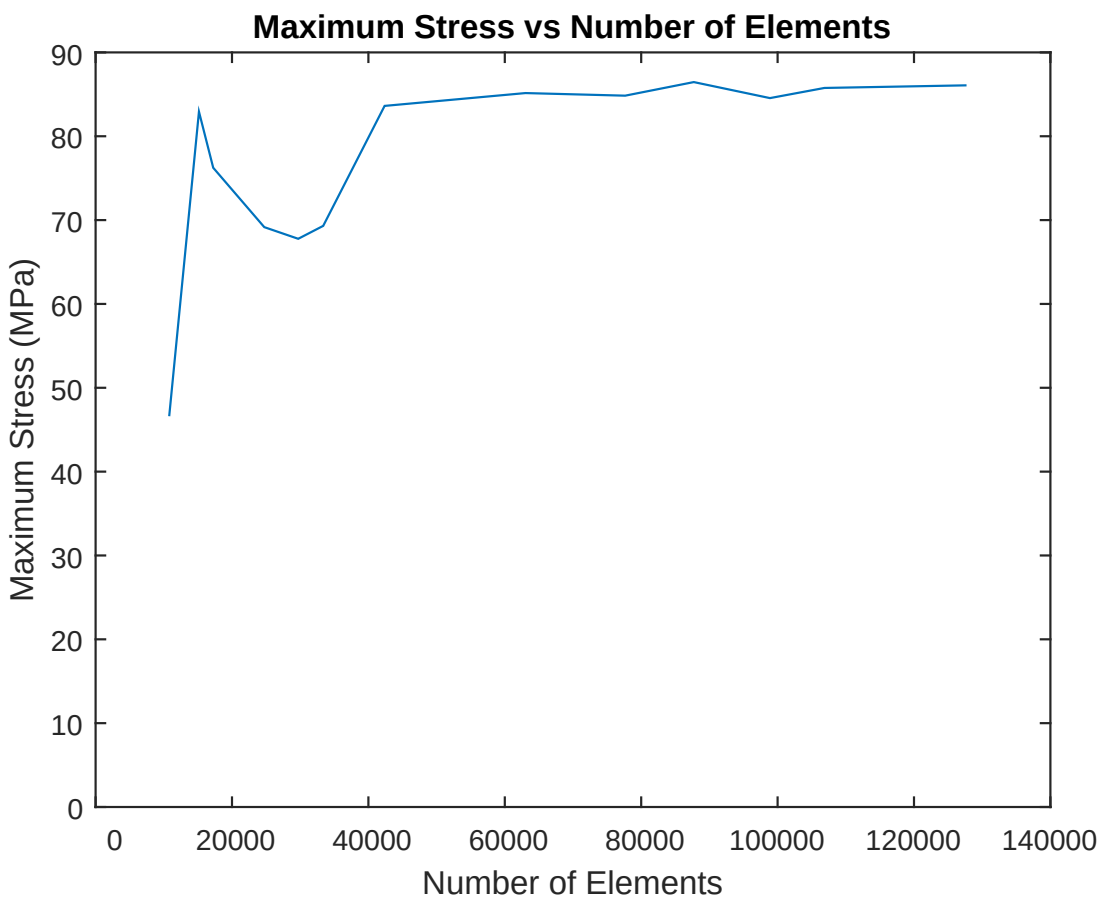

Figure 5.7: Plot of Von Mises stress values vs the number of elements for that simulation

Number of Elements	Absolute Change in Stress Value (%)
10809	n/a
15156	77.43
17247	8.067
24733	9.287
29710	2.010
33373	2.272
42376	20.65
63031	1.830
77652	0.3641
87714	1.910
98879	2.209
106866	1.431
127543	0.3615

Table 5.5: Change in Von Mises stress for varying mesh densities

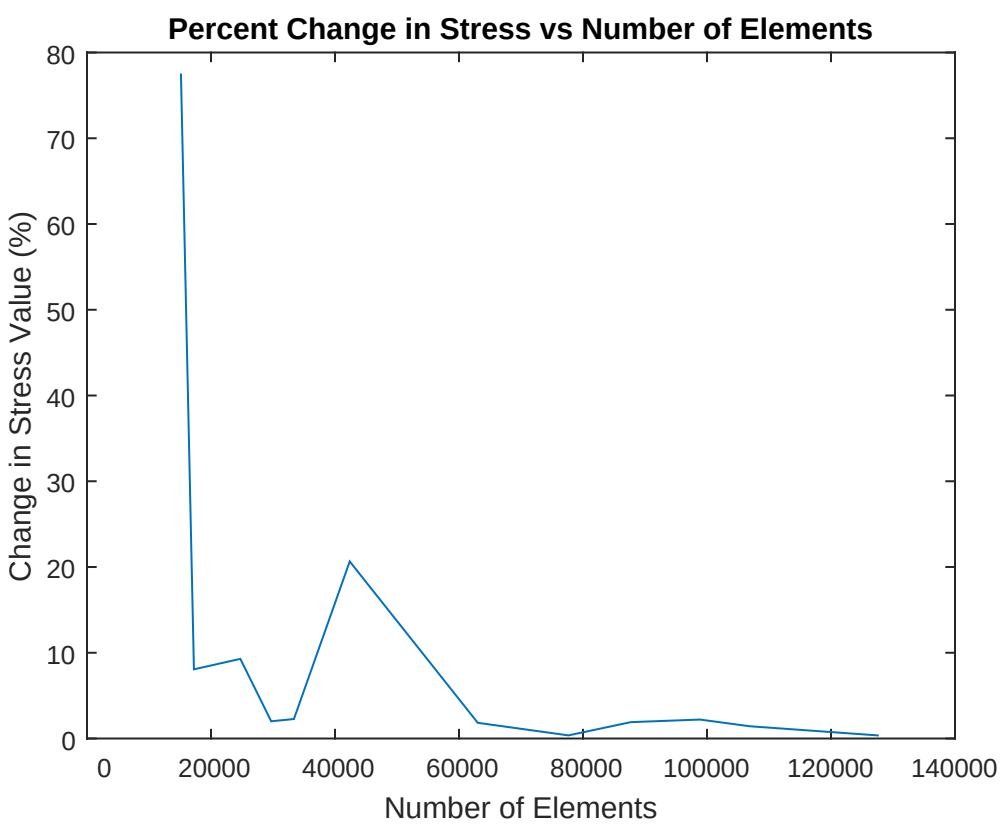

Figure 5.8: Percent error of simulations for consecutive meshes

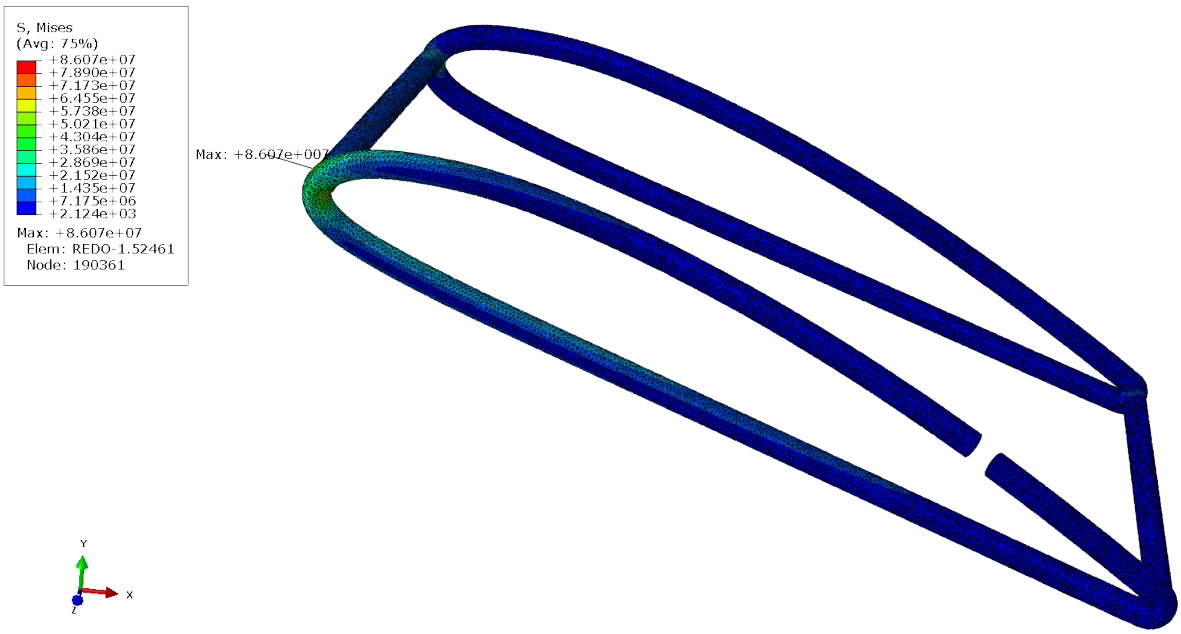

Figure 5.9: Stress state for the meshed wireframe model with 127543 elements

5.3 Full Model Analysis

5.3.1 Analysis Setup

The full propeller model was imported into Abaqus, and the nanocrystalline nickel properties were once again applied to the model. Quadractic tetrahedral elements were used for generating the mesh, as with the double wireframe section model. Using the mesh density from the model with 63031 elements and applying it to the full propeller model results in a mesh with 590523 elements with 1184149 nodes. The model can be seen in Figure 5.10. Since the first wireframe section would be attached to the hub, boundary conditions were applied to the this section to simulate its rigidity, represented as the orange in Figure 5.11. Loads were then applied at each cutout of the remaining wireframe sections as shown in purple in Figure 5.12. They were implemented as a pressure load, again, assuming the actuator applied the load evenly across the wireframe cutout surfaces. The values of the loads applied, and the equivalent actuation force are shown in Table 5.6, with the first wireframe section being the one with boundary conditions applied to it.

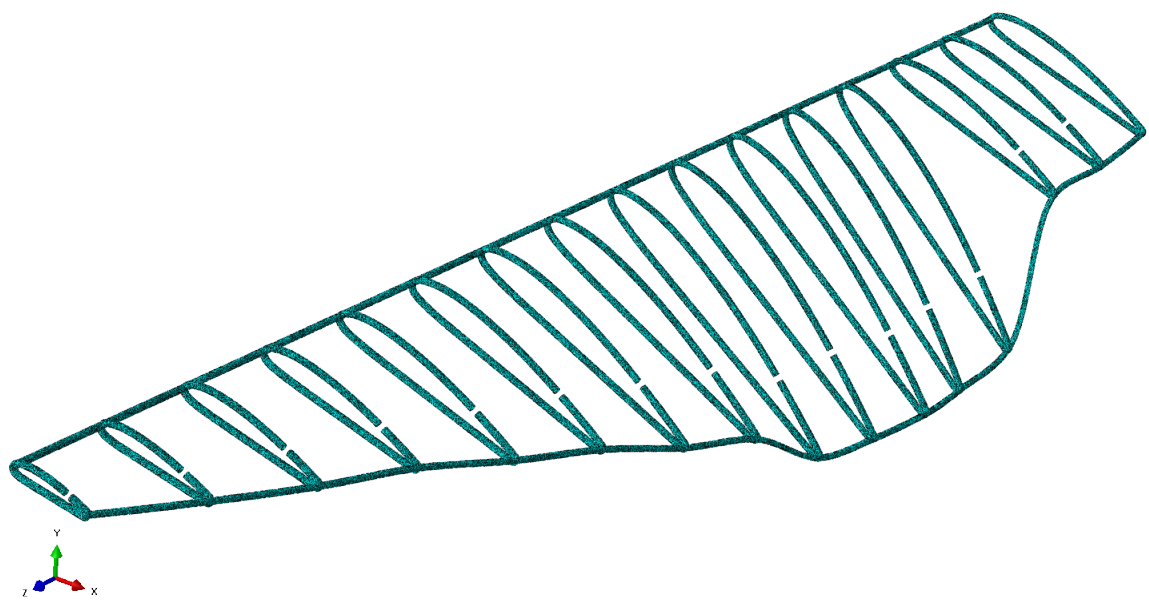

Figure 5.10: View of mesh for the full propeller model

5.3.2 Full Model Results

The results of the simulation can be seen in Figures 5.13 and 5.14. The first thing of note is that the stress level appears to be relatively low throughout the entire structure, however the highest stress level on the contour spectrum is not currently visible. It is then expected that higher stress levels are present on the inner surfaces of the structure. Taking a section cut halfway through the wireframe section at the location of the highest stress level within the structure reveals these higher stress levels. This can be seen in Figure 5.15. Upon further inspection, there exists a large gradient ranging over a very small amount of relatively small elements. This gradient starts from 359 MPa to 2756 MPa. While the upper

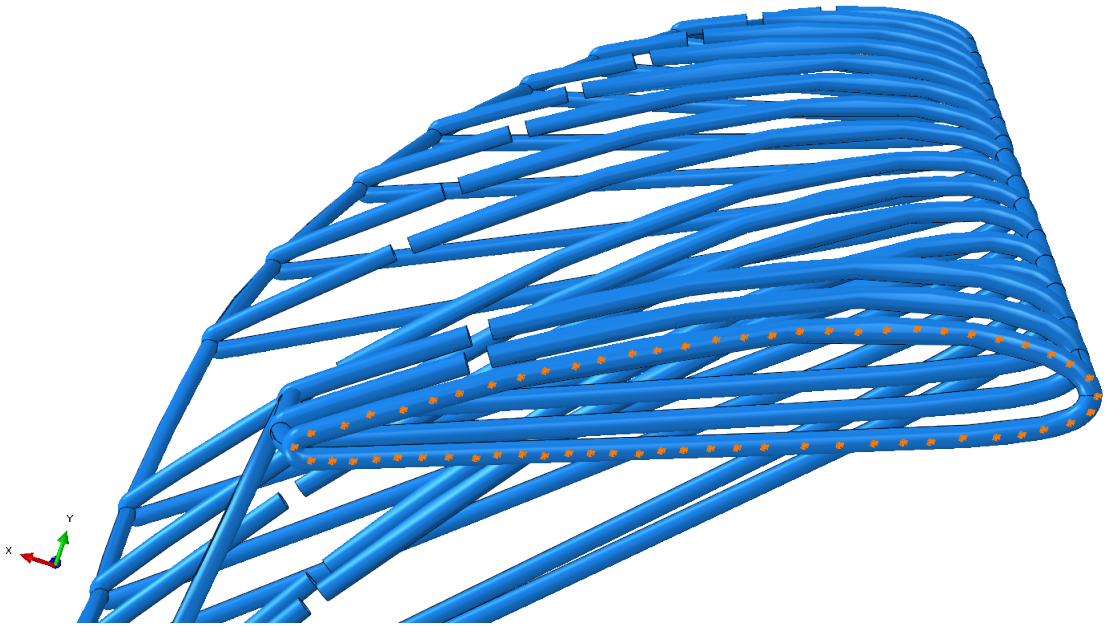

Figure 5.11: Boundary conditions for the full propeller model

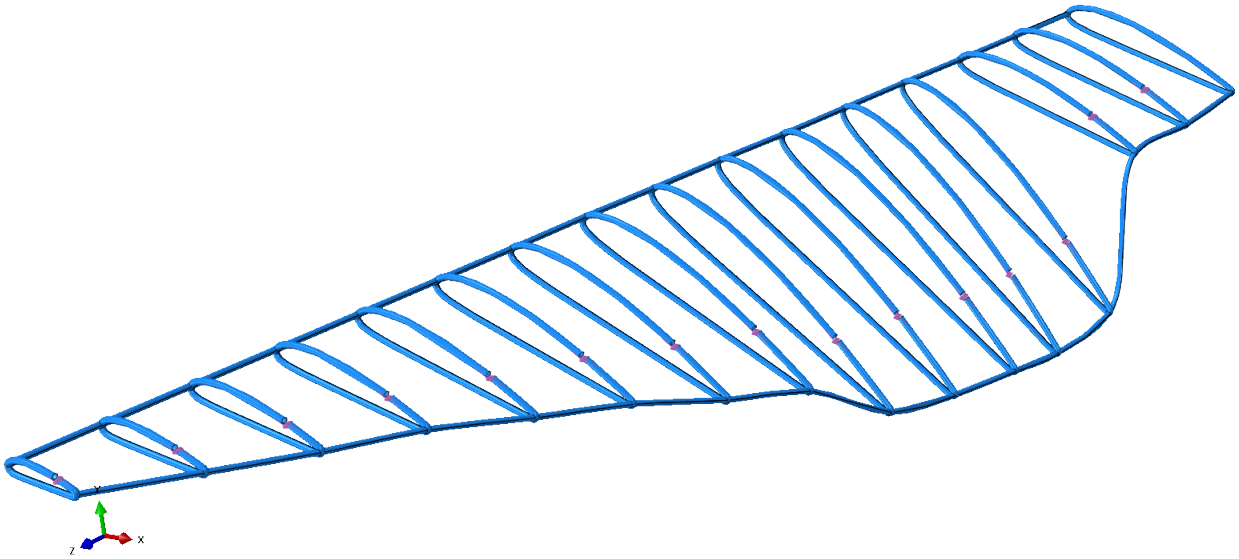

Figure 5.12: Loads applied to the full propeller model

end of this stress contour is well above the yield strength of nanocrystalline nickel, this is likely due to the size of the element and accentuated by rapid geometric changes. This is supported by the fact that this sharp gradient does not occur at any other wireframe section. If this not the case, it could be remedied by slightly increasing the thickness of this section and reducing mismatches in the curvatures of the wireframe section and the wirelike connection. A negative consequence of this would be a lower

Wireframe Section Number	Pressure Applied (MPa)	Equivalent Force (N)
1	n/a	n/a
2	12.7	4.63
3	12.9	4.71
4	40.2	14.7
5	22.5	8.21
6	52.6	19.2
7	53.8	19.6
8	55.1	20.1
9	30.3	11.1
10	22.4	8.17
11	17.9	6.53
12	12.6	4.60
13	11.3	4.12
14	9.10	3.39
15	7.60	2.77
16	5.70	2.08

Table 5.6: Pressures applied to full propeller model and equivalent force

change in twist angle for this section. However, in the current state, this structure would in fact fail catastrophically. Since the stated stress level is much greater than the ultimate tensile strength of the nanocrystalline nickel coating, this excess stress would result in further strain, and ultimately, fracture of the coating. The lower end of this stress contour is also in the same range as the most conservative value of the yield strength of the nanocrystalline nickel, however a stronger coating would overcome this.

Since even the inner surface of the structure remains at the lowest stress contour level, it is valuable to reduce the highest stress contour level by an order of magnitude to have a better sense of the overall stress levels within the structure. This can be seen in Figure 5.16. Inspecting these newly generated contours reveals varying stress levels throughout the structure, which increases at the intersection between the wireframe sections and the wire-like connections running throughout the structure. In addition, the stress levels are higher at the wireframe sections which experience larger changes in their twist angles.

Taking the same section cut as before, but with the new stress contour levels provides a much better understanding of the stress state within the structure. This can be seen in Figure 5.17. The stress rapidly increases right where the wireframe section intersects with the wirelike connection, and also where there is a sharp change in geometry in the same area. This suggests that the high stress state is accentuated by non-smooth curvatures between varying elements, and that the stress could be slightly reduced with improved matching of the curvatures of these elements. It should be noted that all of the stress contours, up to and including the red one, are all well below even the lowest yield strength values for nanocrystalline nickel.

The next significant result is the overall deformation of the structure. The actuation forces cause the trailing edge wire-like connection to displace inwards and upwards. For each individual wireframe section, the amount is relatively small, but the combined effect from all of the sections causes a significant sweep. The contribution to the sweep is greater for the wireframe sections that have a larger actuation force, and thus undergo larger changes in twist angle. While a swept propeller could provide benefits in terms of lift to drag ratio, the model previously used to predict the propeller performance does not take into account any sort of sweep. As a result, the effects of this will be omitted.

In order to determine the change in the twist angles, nodal displacements must be used. However,

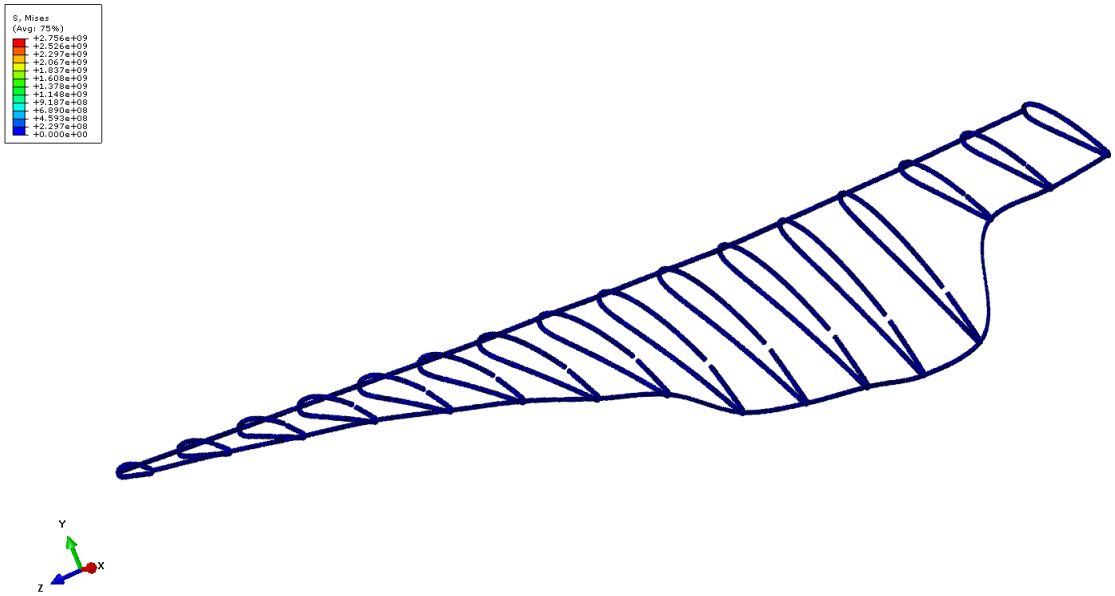

Figure 5.13: Isometric view of full propeller after actuation

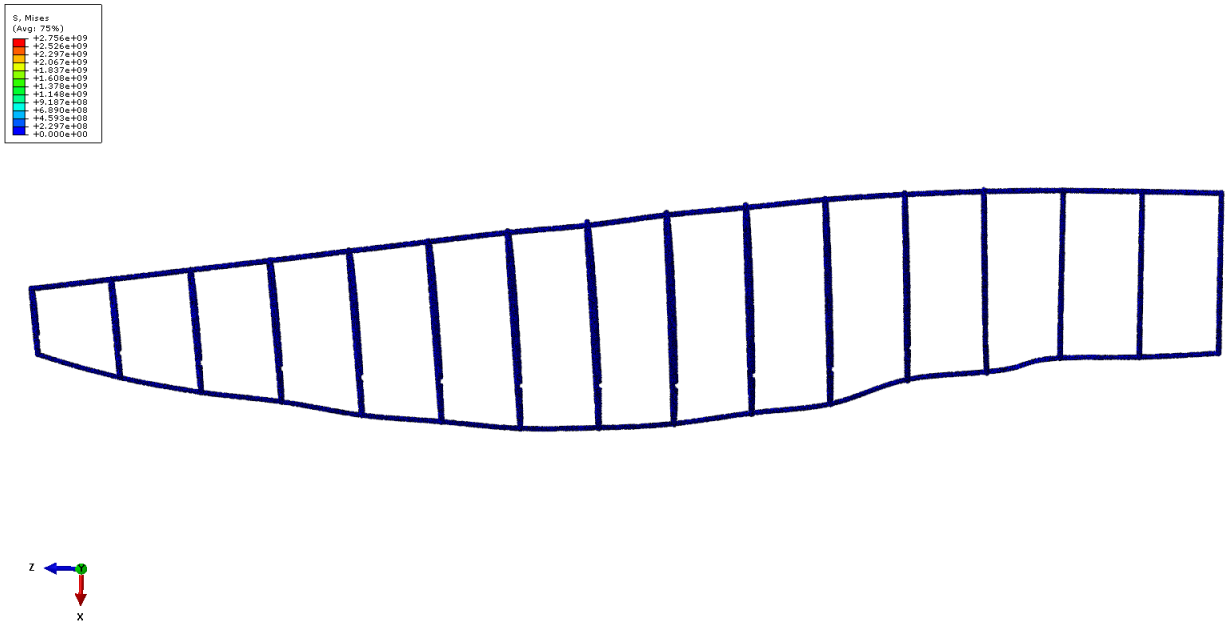

Figure 5.14: Top view of full propeller after actuation

due to the sweep in the model due to the actuation forces, the calculation of this becomes a little less trivial. The sweep causes each individual wireframe section to rotate out of the XZ-plane, otherwise an arctangent calculation using nodal coordinates and displacements could be performed for each wireframe section before and after, followed by a subtraction of the two to determine the change in twist angle. Instead, the twist angle of each wirferame section after the actuation force is applied must be made

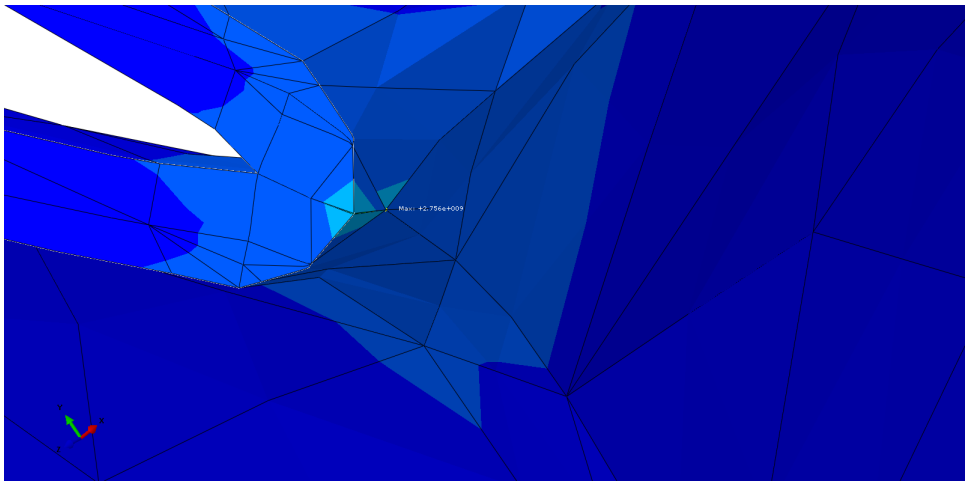

Figure 5.15: Section view cut showing inner surface containing maximum stress location

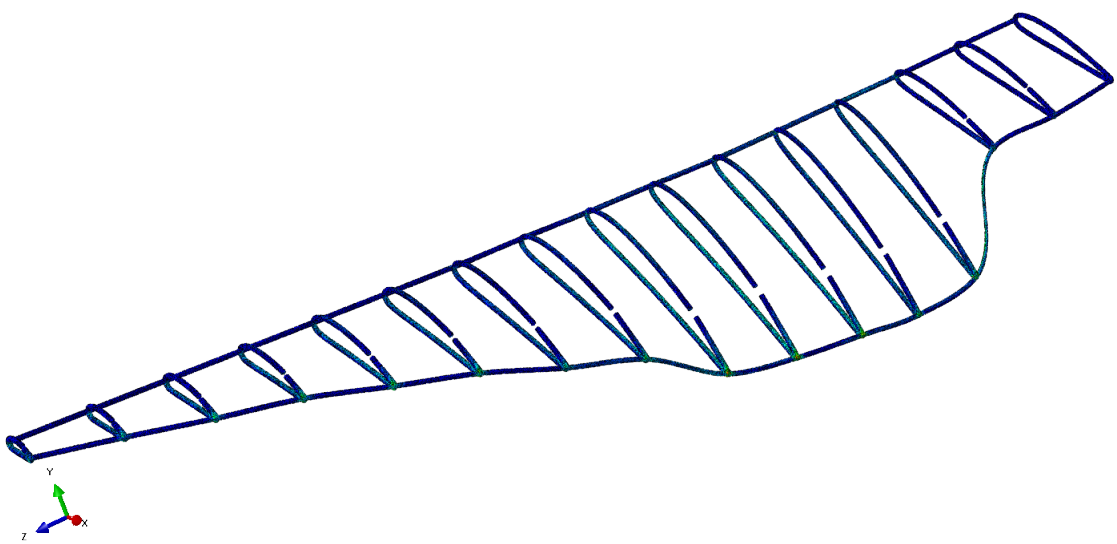

Figure 5.16: Isometric view of propeller with an order of magnitude lower stress limit

relative to a XZ-plane rotated an equal amount to the sweep at each respective section. This can be done by first determining the angle between the chord at each wireframe section and the global X-axis. This can be done using

$$\cos\theta = \frac{\vec{u}\cdot\vec{v}}{||u||||v||}. \tag{5.3}$$

This angle can be used to determine the orientation of a local X-axis by rotation the XZ-plane by this amount about the global Y-axis. Equation 5.3 can be used once again to determine the angle made between the wireframe section and the local XZ-plane generated. This angle is the twist angle after

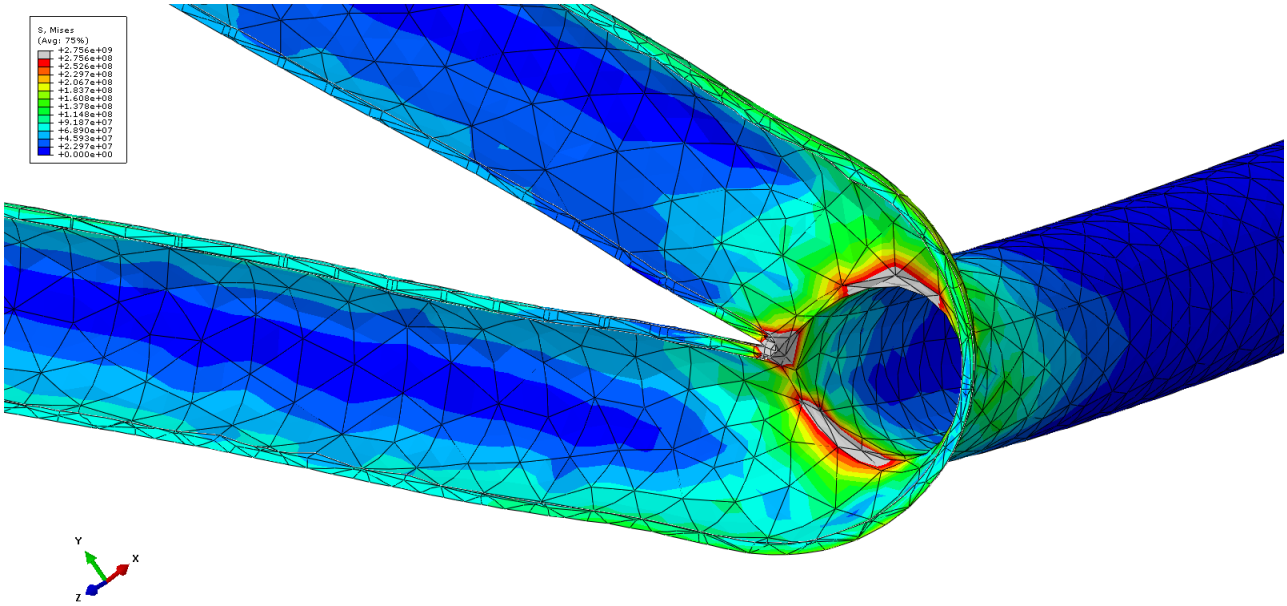

Figure 5.17: Section view cut with a single order of magnitude lower stress limit

actuation. A subtraction between the new twist angle and the original twist angle provides the change experienced by the wireframe section. The results for each wireframe section is shown in Table 5.7.

Wireframe Section Number	Change in Twist Angle (°)	Desired Twist Angle Change (°)
2	1.941	2.098
3	1.923	2.164
4	9.289	9.609
5	5.505	5.546
6	4.067	3.963
7	3.970	3.906
8	3.471	3.511
9	2.250	2.197
10	1.717	1.802
11	1.249	1.355
12	0.984	1.074
13	0.814	0.779
14	0.703	0.602
15	0.498	0.402
16	0.303	0.228

Table 5.7: Twist angles before and after actuation for each wireframe section

All of the actual changes in the twist angle are close to the desired values, but none of the sections match completely. Thus, the benefits gained from morphing the structure would still be present, but reduced. There would exist a combination of actuator forces that would allow for a more accurate change in the twist angle, however this would likely require testing of a physical model.

Chapter 6

Conclusions

This thesis explores the concept of designing a functioning morphing structure using a 3D printed polymer substrate with a nanocrystalline metal coating electrodeposited onto it. The polymer substrate allows for complex shapes to be generated, while the nanocrystalline metal coating provides significant strength for the structure, even if it is a relatively thin coating. It was decided to create a proof of concept design. The application that was chosen was a quadrotor propeller blade. A model was developed in order to predict the behaviour of the propeller from an aerodynamic perspective. An optimal twist profile was then generated for the propeller blade. This profile was used as the basis for exploring various design concepts. Finally, one of the designs was chosen to be evaluated using a detailed finite element analysis.

The model that was developed in order to predict the aerodynamic behaviour of the propeller blade involved using two different frameworks. These are blade element momentum theory and the vortex panel method. The vortex panel method used to geometric inputs from the airfoil in order to determine the coefficients of lift and drag as a result of airflow around the airfoil. This output was then used as an input for the blade element momentum theory, along with assigned discrete section properties for the propeller blade, and predetermined flight characteristics. This model was verified against the performance characteristics of an existing propeller. It was shown that the predicted aerodynamic behaviour from the combined frameworks matched the tabulated values of the propeller chosen fairly well.

The next step was moving ahead with an aerodynamic optimization. For this, a NACA 2412 airfoil was chose to be the base airfoil profile across the whole propeller blade. Chord properties were assigned to discrete sections along the propeller blade span. A gradient based optimization was performed using the developed model, maximizing the lift generation by determining the optimal twist profile for each discrete section. Once the profile was generated, it was used as an input into the developed model to predict the aerodynamic behaviour. It was found that the behaviour of the generated propeller blade is in a reasonable range when compared to other available propellers, providing confidence in the optimization results.

The generated twist profile was then used in conjunction with the NACA 2412 airfoil to bring create a set of discrete airfoil sections. This was the basis of the design concepts explored. Three separate designs were created and examined. Each design provides different benefits as well as drawbacks. These include, but are not limited to, level of actuation, overall mass, structural stiffness, 3D printing capability, electrical component embedding potential, and difficulty of electrodeposition. Rough models were created

for each separate design in order to give a better understanding of the design process, as well as the mechanisms by which they function. The design were refined in order to improve their viability, and make them

The rigid wireframe body was chosen in order to perform a finite element analysis using Abaqus. A robust, detailed model was created in Autodesk Inventor, reflecting the details discussed. An analysis was done on a single wireframe section to give an understanding of the magnitude of the actuation forces required, as well as to provide the opportunity to perform a mesh convergence analysis. This showed that the force required from an actuator is in a range that can be provided by available actuators. An appropriate mesh density was determined that would be applied to the full propeller blade model through a mesh sensitivity analysis. An analysis on the full model was then performed. This showed the level of actuation required by each section, as well as that the structure is able to withstand the forces acting upon it due to the actuation.

The next steps would be to create a physical model by 3D printing a substrate, electrodepositing nanocrystalline nickel on top, and removing the underlying substrate. Selection of appropriate actuators would need to be done and installed onto the physical model. Testing would then be done in order to determine the force required to achieve the exact twist angle that is desired for maximum aerodynamic benefits. The effect of the sweep induced due to the morphing would also need to be investigated to ensure that it does not hinder the lift generation of the propeller.

Bibliography

[1] Jirout Reklamní Agentura. Model motors, 2015. [Online; accessed 6-August-2020].

[2] International Air Transport Association. Climate change & CORSIA fact sheet, 2018. [Online; accessed 6-August-2020].

[3] Silvestro Barbarino, Onur Bilgen, Rafic M Ajaj, Michael I Friswell, and Daniel J Inman. A review of morphing aircraft. *Journal of Intelligent Material Systems and Structures*, 22(9):823–877, 2011.

[4] Hilary Bart-Smith and Philip E Risseeuw. High authority morphing structures. In *ASME 2003 International Mechanical Engineering Congress and Exposition*, pages 399–403. American Society of Mechanical Engineers, 2003.

[5] Boeing. Boeing 787 from the ground up, 2009. [Online; accessed 6-August-2020].

[6] J.B. Brandt, R.W. Deters, G.K. Ananda, and M.S. Selig. UIUC propeller database, University of Illinois at Urbana-Champaign. [Online; accessed 6-August-2020].

[7] Ruby Calzada. AFTI F-111, 2017. [Online; accessed 6-August-2020].

[8] Lisa Case, Zachary Kreiner, John Redmond, and Brian Trease. Shape memory alloy shape training tutorial, 2004. [Online; accessed 6-August-2020].

[9] F Ebrahimi, G.R Bourne, M.S Kelly, and T.E Matthews. Mechanical properties of nanocrystalline nickel produced by electrodeposition. *Nanostructured Materials*, 11(3):343–350, 1999.

[10] U. Erb, A.M. El-Sherik, C.K.S. Cheung, and M.J. Aus. Nanocrystalline metals, July 18 1995. US Patent 5,433,797.

[11] H. Glauert. *The Airscrew: Blade Element Theory*. Cambridge Science Classics. Cambridge University Press, 1983.

[12] LM Gordon, BA Bouwhuis, M Suralvo, JL McCrea, G Palumbo, and GD Hibbard. Micro-truss nanocrystalline Ni hybrids. *Acta Materialia*, 57(3):932–939, 2009.

[13] Edwin P.A. Heinze. The Makhonine way. *Flight International*, May 1932.

[14] Larry L Howell. *Compliant Mechanisms*. John Wiley & Sons, 2001.

[15] Larry L Howell, Spencer P Magleby, and Brian Mark Olsen. *Handbook of compliant mechanisms*. Wiley Online Library, 2013.

[16] RG Hutchinson, N Wicks, AG Evans, NA Fleck, and JW Hutchinson. Kagome plate structures for actuation. *International Journal of Solids and Structures*, 40(25):6969–6980, 2003.

[17] APC International. Stripe actuators, 2016. [Online; accessed 6-August-2020].

[18] Jaronie Mohd Jani, Martin Leary, Aleksandar Subic, and Mark A Gibson. A review of shape memory alloy research, applications and opportunities. *Materials & Design*, 56:1078–1113, 2014.

[19] Jari Juuti, Krisztián Kordás, R Lonnakko, V-P Moilanen, and S Leppävuori. Mechanically amplified large displacement piezoelectric actuators. *Sensors and Actuators A: Physical*, 120(1):225–231, 2005.

[20] A.M. Kuethe and C.Y. Chow. *Foundations of aerodynamics: bases of aerodynamic design*. Wiley, 1986.

[21] AT Lausic, CA Steeves, and GD Hibbard. Effect of grain size on the optimal architecture of electrodeposited metal/polymer microtrusses. *Journal of Sandwich Structures and Materials*, 16(3):251–271, 2014.

[22] Zhen Luo, Liping Chen, Jingzhou Yang, Y Zhang, and K Abdel-Malek. Compliant mechanism design using multi-objective topology optimization scheme of continuum structures. *Structural and Multidisciplinary Optimization*, 30(2):142–154, 2005.

[23] J Ma, I Karaman, and Ronald D Noebe. High temperature shape memory alloys. *International Materials Reviews*, 55(5):257–315, 2010.

[24] H. A. Mettam. The pterodactyl story. *Flight International*, Mar 1970.

[25] Noliac. Piezo definitions, 2011. [Online; accessed 6-August-2020].

[26] International Civil Aviation Organizaton. ICAO environmental report 2016, 2016. [Online; accessed 6-August-2020].

[27] Kazuhiro Otsuka and Xiabing Ren. Physical metallurgy of Ti–Ni-based shape memory alloys. *Progress in Materials Science*, 50(5):511–678, 2005.

[28] AYN Sofla, DM Elzey, and HNG Wadley. A rotational joint for shape morphing space truss structures. *Smart Materials and Structures*, 16(4):1277, 2007.

[29] AYN Sofla, DM Elzey, and HNG Wadley. Shape morphing hinged truss structures. *Smart Materials and Structures*, 18(6):065012, 2009.

[30] 3D Systems. VisiJet M3 crystal 3D material, 2016. [Online; accessed 6-August-2020].

[31] Terrence A Weisshaar. Morphing aircraft technology-new shapes for aircraft design. Technical report, Purdue University Lafayette IN, 2006.